Title

Genome-wide association study in Collaborative Cross mice revealed a skeletal role for *Rhbdf2*

Authors

Roei Levy[1,2], *Clemence Levet*[3], *Keren Cohen*[1], *Matthew Freeman*[3], *Richard Mott*[4], *Fuad Iraqi*[5], *Yankel Gabet*[1]

Affiliations

[1] Department of Anatomy and Anthropology, [2] Department of Human Molecular Genetics and Biochemistry, and [5] Department of Clinical Microbiology and Immunology, Sackler Medical School, Tel Aviv University. [3] Dunn School of Pathology, South Parks Road, Oxford OX1 3RE. [4] UCL Genetics Institute, University College London, Gower St., London, WC1E 6BT, UK.

Abstract

A growing concern that overshadows the increased life expectancy developed countries have been witnessing during the last decades is an accompanying bone loss, which often manifests as osteoporosis. Despite ongoing efforts in utilizing genomic data to fully map the genes responsible for bone remodeling, a detailed picture remains to be desired. Here we took advantage of the phenotypic and genetic diversity innate in Collaborative Cross (CC) mice to identify genetic variants associated with microstructural bone characteristics.

We gauged several key femoral microarchitecture features of the femoral bone: bone volume fraction (BV/TV), number (Tb.N), thickness (Tb.Th), structural morphometric index (SMI) and spacing (Tb.Sp) of the trabecula, and thickness (Ct.Th) and volumetric bone mineral density (vBMD) of the cortex, to uncover possible genes by which these might be affected.

We found 5 loci associated with 6 of the traits – BV/TV, Tb.N (one mutual locus), Tb.Th, Tb.Sp, vBMD, and Ct.Th (one locus per trait). The broad-sense heritability of these traits ranged between 50 to 60%. The cortical traits were especially sensitive to confounders, such as batch, month and season. We refined each locus by combining information mined from existing databases with that obtained from the known ancestry of the mice, to shortlist potential candidate genes.

We found strong evidence for new candidate genes, in particular, *Rhbdf2*. Using *Rhbdf2* knockout mice, we confirmed its strong influence on bone microarchitecture; *Rhbdf2*$^{-/-}$ mice exhibited strikingly heightened BV/TV and Tb.N, heightened SMI and Ct.Th, lowered Conn.D and Tb.Sp, and unaffected Tb.Th and vBMD, compared with wild type mice. High-resolution bone microarchitecture imaging of the CC population enabled us to further dissect the genetic makeup of bone morphology, and demonstrate conclusively that *Rhbdf2* reduces the number and volume of the femoral trabecula.

Introduction

Osteoporosis is the most common bone disease in humans, affecting nearly half the US and European population over the age of 50 years. With the globally increasing life expectancy, osteoporosis and related bone fractures are becoming a pandemic

health and economic concern. By 2050, the world-wide incidence of hip fractures is expected to increase by 2.5 to 6 fold (Burge et al. 2007; Dhanwal et al. 2011). Importantly, the mortality rate in the 12 months following bone fracture is as high as 20% (Center et al. 1999). Risk of fracture is determined largely by bone density and quality/strength, which are the end result of peak values achieved at skeletal maturity and subsequent age and menopause-related bone loss. Genetic factors have a major role in determining the wide range in the so-called "normal" peak bone mass. Measures of bone status are inherently complex traits, as opposed to Mendelian traits; i.e. they are controlled by the cumulative effect and interactions of numerous genetic loci and environmental factors.

Genome-wide association studies (GWAS), including a large meta-analysis, have identified more than 50 loci associated with bone mineral density (BMD) (Mizuguchi et al. 2004; Richards et al. 2008; Styrkarsdottir et al. 2008; Trikalinos et al. 2008; Estrada et al. 2012; Paternoster et al. 2010, 2013). However, many other genes that were experimentally associated with bone mass were not confirmed by GWAS in human cohorts (Jovanovich et al. 2013; Hsu and Kiel 2012; Styrkarsdottir et al. 2013). This suggests that the BMD phenotype does not capture the structural complexity of the bone; there may be other relevant bone phenotypes not yet studied in human GWAS (Hsu and Kiel 2012), which hitherto have generally relied on areal bone mineral density (aBMD) as the sole bone feature. aBMD measured by dual energy x-ray absorptiometry (DXA) is a two dimensional projection that cannot measure bone size, individual bone compartments' shape (whether trabecular or cortical) or underlying microstructure, and thus likely conceals important features which are assumed to be controlled by unique genetic determinants. Indeed, there is a growing body of evidence that argues for distinct genetic influences of the cortical

and trabecular bone and thus they should be accordingly distinguished. (Paternoster et al. 2010; Estrada et al. 2012). A recent GWAS in the Collaborative Cross (CC) mice based on DXA failed to find any heritability of BMD (Iraqi et al. 2014), whereas another report based on the same mouse panel showed highly significant heritability levels in most of the cortical and trabecular microstructural parameters measured by micro-computed tomography (μCT)(Levy et al. 2015a).

Traditional peripheral quantitative CT (pQCT) has the capacity to distinguish between the cortical and trabecular bone compartments, but it lacks the required resolution to detect microstructural differences. A recent report based on high resolution pQCT (HR-pQCT) data in humans, identified two novel bone-related loci, thus far undetected by DXA and pQCT-based GWAS (Paternoster et al. 2010). Another (Karasik et al. 2016), found strong genetic correlations between 1047 adult participants of the Framingham heart study, therefore indicating that the heritability of bone microstructure constitutes a phenotypic layer which is at least partially independent of DXA-derived BMD. Like HR-pQCT studies in humans, understanding the genetic regulation of bone microstructural parameters using μCT in small animals is likely to identify genetic factors distinct from those previously identified for DXA-derived traits.

The CC mouse panel is designed to provide high resolution analysis of complex traits, with particular emphasis on traits relevant to human health (Threadgill et al. 2002; Churchill et al. 2004). This unique resource currently consists of a growing number of recombinant inbred lines (RIL) generated from full reciprocal breeding of eight divergent strains of mice (Collaborative Cross Consortium 2012). In contrast to commonly used laboratory mouse strains, the ancestry of the CC lines

includes wild-derived inbred strains that encompass genetic variations accumulated over ~1 million years (Keane et al. 2011); more than 50 million single nucleotide polymorphisms segregate in founders of the CC. The high genetic diversity means that QTLs can be mapped using this panel that would have been invisible in a population that involved only classical strains (Roberts et al. 2007; Durrant et al. 2011b).

This claim is substantiated in a recent study that identified a genome-wide significant association between *Oxt* (oxytocin) and *Avp* (vasopressin) and skeletal microarchitecture in CC mice. Here, we identified a novel gene, *Rhbdf2*, associated with cortical and trabecular bone structure and validated its regulatory role in a specific knockout model. This exemplifies the effectiveness and relative ease by which a GWAS with a small CC population can associate a bone-related function to novel genes, and to reveal overlooked key players in the development of bone pathologies.

Results

CC lines widely differ in bone microarchitecture traits

We examined the variation in femoral cortical and trabecular microstructure between 34 unique CC lines totaling in 174 mice (71 females and 103 males, with an average of 4.25 mice per line). In the trabecular bone compartment we measured bone volume fraction (BV/TV), trabecular number (Tb.N), thickness (Tb.Th), connectivity (Conn.D), and spacing (or separation; Tb.Sp), as well as structural morphometric index (SMI) of the trabecular framework. In the mid-diaphyseal cortex, we recorded cortical thickness (Ct.Th) and volumetric bone mineral density (vBMD). (see

(Bouxsein et al. 2010) for µCT nomenclature.) These traits were approximately normally distributed; BV/TV ranged from 0.017 to 0.26 (i.e. 1.7% to 26%; mean = 10.2%); Tb.N from 0.52 to 6.11 mm^{-1} (mean = 2.7 mm^{-1}); Tb.Th from 31 to 69 µm (mean = 47 µm); Conn.D from 10.9 to 268.3 mm^{-3} (mean = 104.2 mm^{-3}); SMI from 0.6 to 3.3 (mean = 2.3); Tb.Sp from 0.16 to 0.7 mm (mean = 0.33 mm); Ct.Th from 0.14 to 0.29 mm (mean = 0.2 mm); and vBMD from 402.5 to 809.2 $mgHA/cm^3$ (mean = 581.1 $mgHA/cm^3$). Fig. 1 shows representative cortical (IL-785 vs IL-2689) and trabecular (IL-2452 and IL-1513) µCT images taken from two mice with distinct cortical (Fig. 1A) and trabecular (Fig. 1B) characteristics. Color-codes on the graphs in Fig. 2 indicate Duncan's least significance range (LSR), which dictates whether the mean value of a line, or a group of lines, for a given trait differs to a degree of at least *P*-value < 0.001 from any other group. LSR allows for a visual representation of the heterogeneity amongst the lines.

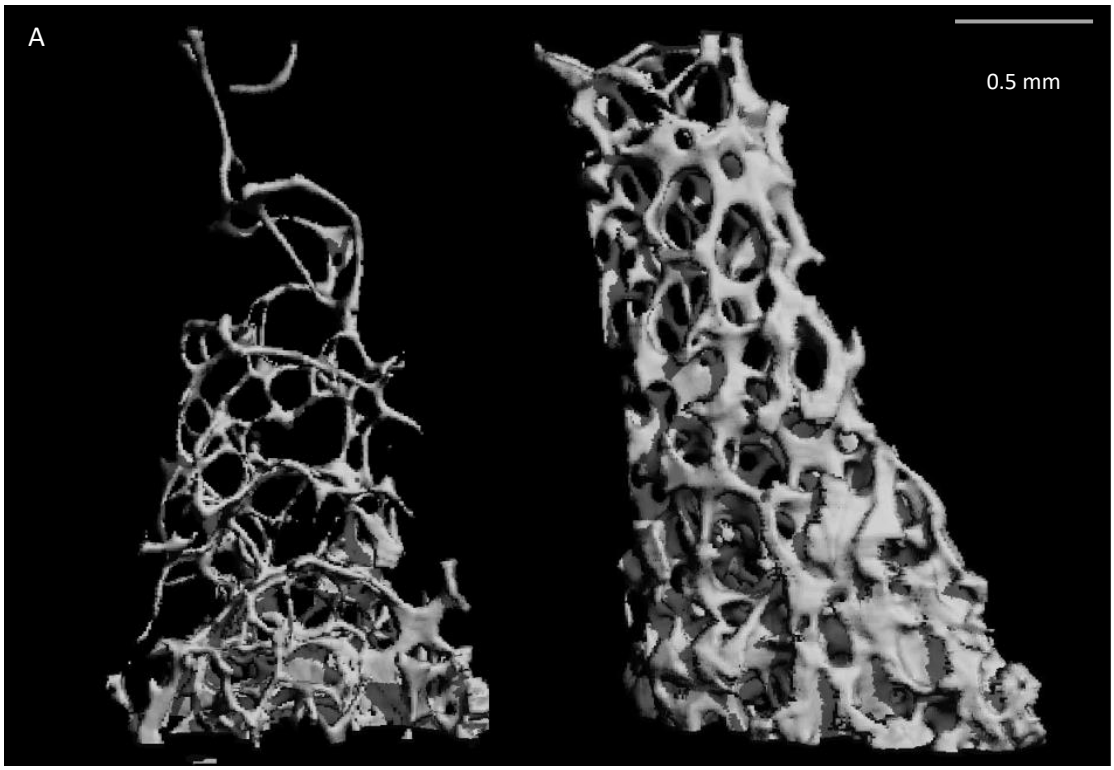

Figure 1. µCT images of trabecular and cortical bone of the femora of representative CC mice. **(A)** Trabecular bone. Left: IL-2452, Right: IL-1513. **(B)** Cortical bone. Left: IL-785, Right: IL-2689.

With 11 distinct groups, vBMD (Fig. 2B) is the most heterogeneous trait, while SMI and Conn.D are the least, with only 3 significantly distinct groups (Fig. 2A). Notably, the heterogeneity of females is greater than that of males for cortical traits but milder for trabecular traits. (Figs. S1A1, 2 for males and S1B1, 2 for females).

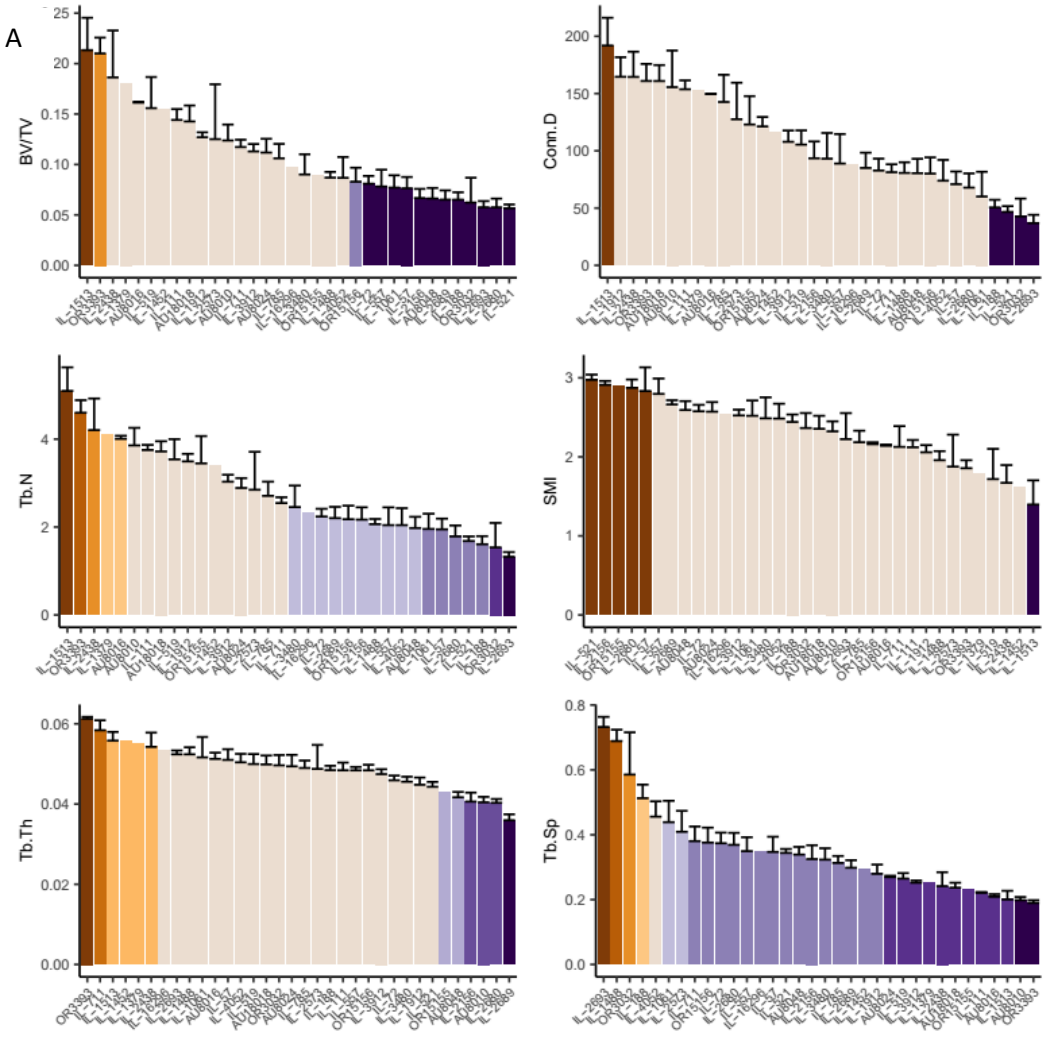

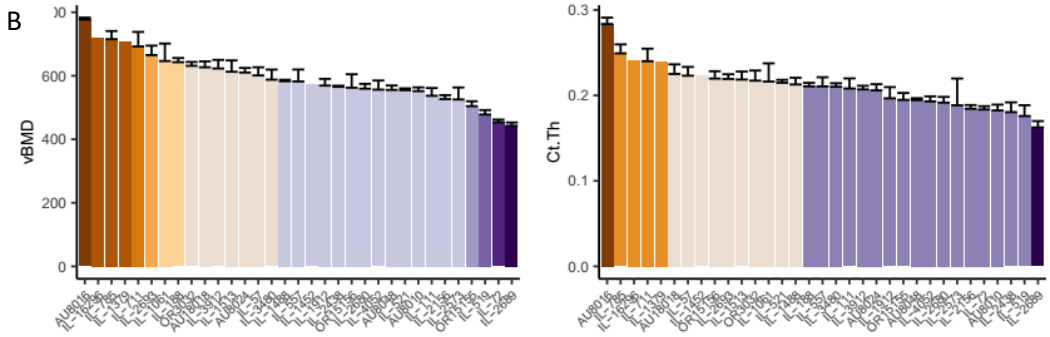

Figure 2 Trabecular and cortical traits distributions across the CC lines. X-axis is the lines, y-axis is the trait means **A**. From top left, counter-clockwise: BV/TV (%), Tb.N (mm^{-1}), Tb.Th (um), Conn.D (mm^{-3}), SMI, and Tb.Sp (mm). **B**. Left, vBMD ($mgHA/cm^3$), right, Ct.Th (mm). Color codes group line(s) which significantly differ from other groups. Lines are ordered inconsistently among the traits, according to trait-specific descending order. Refer to Table S3 for more details.

To examine the inter-dependency between the traits, we assessed the correlation between all the measured parameters, in a pairwise fashion using Pearson's correlation test. The strongest correlation was between BV/TV and Tb.N (Pearson's $r = 0.94$), in line with our previous findings (Levy et al. 2015b), while the weakest was between Tb.N and vBMD ($r < 0.01$). There was also a moderately high correlation between Ct.Th and Tb.Th ($r = 0.61$; and see Table S1). The correlation between sexes for each trait (Table 1) ranged from $r = 0.75$ (Tb.Sp) to $r = 0.20$ (Ct.Th). Body weight (range = 17.4 - 35.0 gr) did not significantly correlate with any of the traits ($r = 0.01$ for Conn.D to $r = 0.19$ for Ct.Th; data not shown). After separating males from females the correlation slightly increased, yet remained low. Weak correlation was found between weight and Tb.N, SMI, and Ct.Th for females

(Pearson's r = -0.20, 0.23, and 0.25 respectively), and between weight and Tb.Th and Tb.Sp (Pearson's r = 0.25 and -0.25) for males.

While in most lines the traits' correlations were predictive of a given line's rank, in others a less expected pattern was observed; e.g., IL-1513 displayed unusually extreme phenotypes for all trabecular traits and was at the higher end for BV/TV, Tb.N, Tb.Th, and Conn.D and at the lower end for SMI and Tb.Sp, but IL-188 was more discordant between these same traits (Fig. 2 and Table S3), illustrating unexpected co-variation of the traits in the CC.

Heritability and confounder-control

We quantitated the effects of the covariates sex, age, batch, month, season, year, and experimenter on each trait. Age ranged from 9 (n=6) to 13 (n=9) weeks and the mice were dissected in 20 batches over a three-year course across 8 months during winter, spring and summer, by two experimenters. Whereas age alone had no effect on any trait, sex affected only Ct.Th; batch affected Tb.Th, vBMD, and Ct.Th; month affected Tb.Sp, vBMD, and Ct.Th; season and year affected vBMD and Ct.Th; and Tb.Th and Ct.Th were affected by experimenter. The cumulative effect of the covariates' pairwise interactions was noted for Tb.Th, SMI, vBMD, and Ct.Th. (Table S2).

We then estimated the broad-sense heritability (H^2) of each trait among the CC lines, which includes additive and non-additive epistatic effects and gene-environment interactions. The greatest H^2 is seen for Tb.N (0.63, logP = 13.76; where logP stands for the negative 10-base logarithm of the P value and tests the null hypothesis that the heritability is zero), and the smallest for Ct.Th (0.51, logP = 7.63).

We calculated the heritability for the mean values in each line to get a better representation of the percentage of genetic contribution to the phenotypic heterogeneity by incorporating H^2 and the average number of lines (Atamni et al. 2016). This defines H^2n, which is directly proportional to H^2 (Methods; Table 1) and ranges between 82 (Ct.Th) and 88% (Tb.N and Tb.Sp).

Table 1 Heritability, sex correlations, and covariate interactions for trabecular and cortical traits

Trait	H^2	logP	H^2n	Sex Cor.	Interactions %
BV/TV	0.61	12.43	0.87	0.6695754	-
Tb.N	0.63	13.76	0.88	0.7628464	-
Tb.Th	0.54	9.08	0.83	0.7039887	34.70
Conn.D	0.56	9.90	0.84	0.5188039	-
SMI	0.55	9.43	0.84	0.2984166	26.02
Tb.Sp	0.63	13.45	0.88	0.754563	-
vBMD	0.62	12.15	0.87	0.6268818	53.92
Ct.Th	0.51	7.63	0.82	0.2055684	41.07

H^2 is the broad-sense heritability (which includes epistatic and environmental influences); logP is the negative 10-base logarithm of the P-value; H^2n is the line-mean heritability; Sex Cor. Is the sex correlation of each trait; and interactions % refers to the relative contribution of the cumulative covariate-interactions, which include sex, age, batch, month, season, year, and experimenter (see table S2) .

Overall the cortical traits seemed more prone to covariate variation; they were particularly sensitive to sex, batch, and season. This stands in contrast to our previous results (Levy et al. 2015b) where BV/TV, Tb.N, and Conn.D displayed a profound sex effect, although there cortical traits were not measured. This means there is a deeper, complex layer of sex effect dependent upon cooperative environmental and genetical factors which requires further work to fully comprehend.

Association analysis for microarchitectural traits highlights 5 QTLs

We first measured statistical association between each trait and the founder haplotype at each locus in the genome. Association analyses of the cortical and trabecular traits to the haplotypes segregating in the CC (as defined by the ~70 K MegaMuga SNPs) yielded 5 distinct QTLs. For BV/TV and Tb.N we recognized a marked peak at a locus of length ~0.45 Mb between 116.5 and 116.9 Mb on chromosome 11, with peak logP values of 7.6 and 6.8, which extended above the 99th percentile permutation-threshold by 2.7 and 1.94 logP units, respectively. In Tb.Th, Tb.Sp, Ct.Th, and vBMD we identified different QTLs on chromosomes 4, 5, 4 and 3, with logPs of 8.0, 9.4, 8.2, and 9.8, respectively, above threshold (Fig. 3 and Table 2). To account for false positive results we kept the false discovery rate (FDR) at 1% for each scan, by employing the Benjamini–Hochberg multiple testing procedure on the logPs of the haplotype associations to the traits. Conn.D and SMI lacked significant peaks above the stringent permutated threshold and thus were not further analyzed (Fig. 3), but Conn.D displayed a borderline peak in a region that matches the peak identified for BV/TV and Tb.N. The 5 QTLs we describe are hereafter referred to as *Trl* (trabecular related locus) 7-9, and *Crl* (cortical related locus) 1-2 (respectively for BV/TV and Tb.N, Tb.Th, Tb.Sp, Ct.Th, and vBMD, and in keeping with our previous report (Levy et al. 2015a) that introduced *Trl* 1-6). The 95% widths of the confidence intervals ranged from 6.4 to 15.6 Mb for the *Trl*s, and were between 8.5-10.8 Mb for the *Crl*s (Table 2 and Fig. S2).

We measured the contribution of each CC founder to the QTLs, relative to the wild-derived strain WSB/EiJ (Fig. 4). *Trl*7 is mostly affected by the classic laboratory strains 129S1/SvImJ, NOD/LtJ, and NZO/HiLtJ; notably, the other traits were more strongly driven by the following wild strains: *Trl*8 and *Crl*2 by PWK/PhJ; *Trl*9 by WSB/EiJ; and *Crl*1 by CAST/Ei.

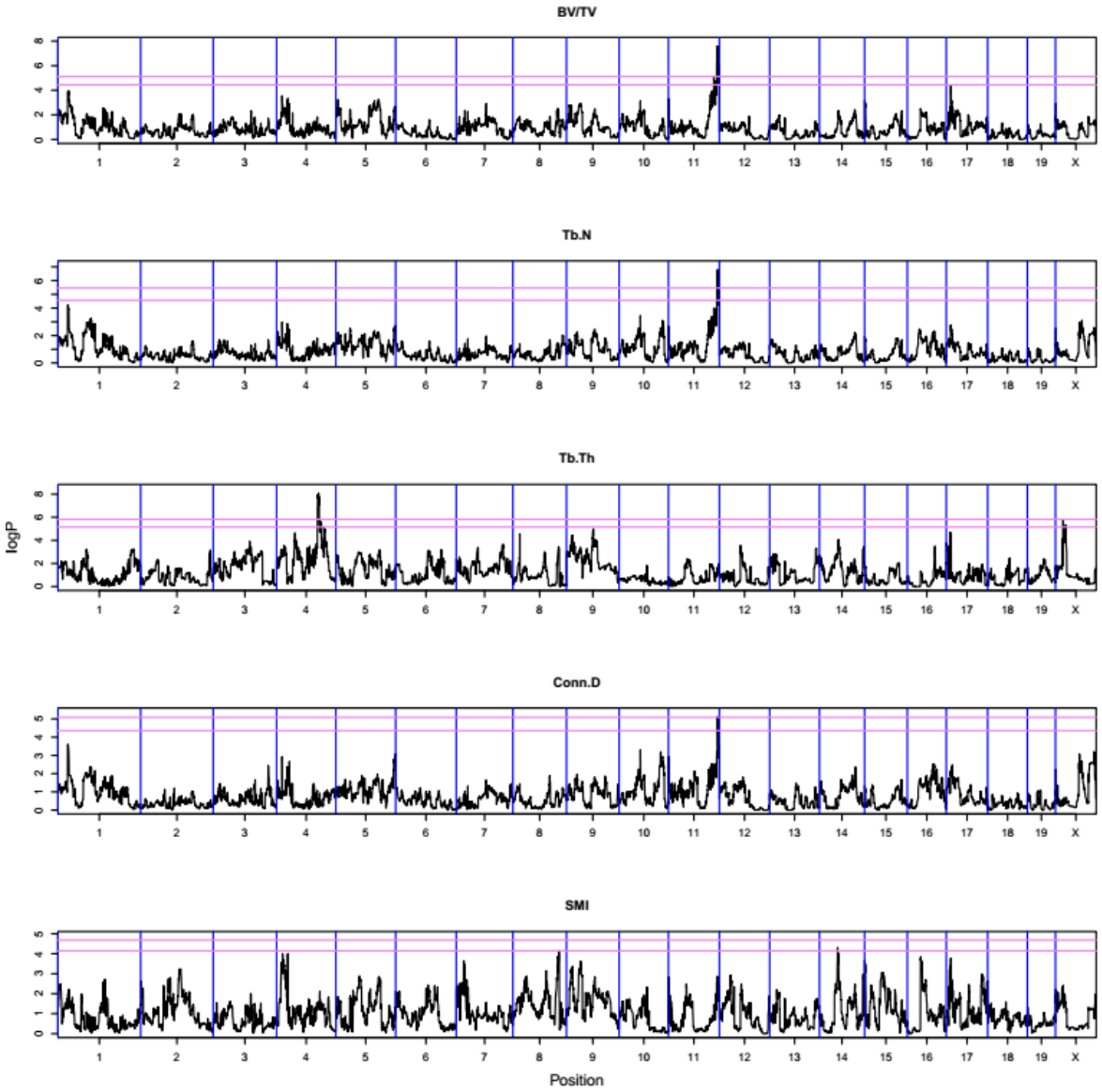

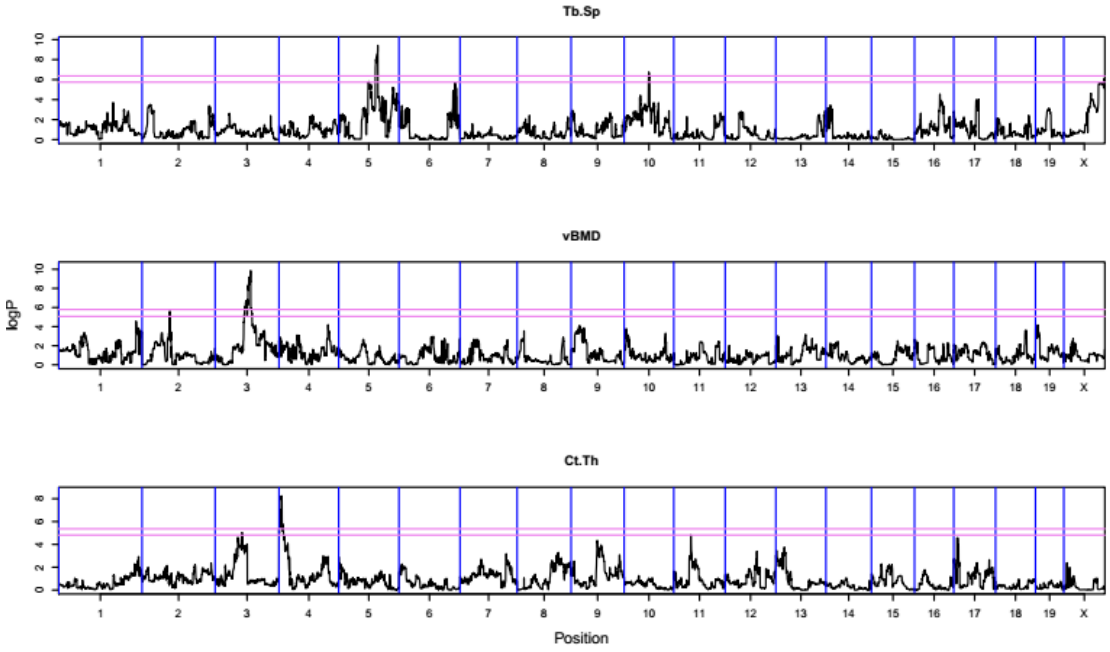

Figure 3 Haplotype association maps for the trabecular and cortical traits. X-axis is the position on the chromosome, y-axis is the –logP value of the association. Lower threshold represents the 95th percentile of 200 simulations, and top represents the 99th percentile. Loci above the 99% cut-off were further investigated. From top to bottom: BV/TV, Tb.N, Tb.Th, Conn.D, SMI, Tb.Sp, vBMD, and Ct.Th

For *Trl7* we found that the majority of lines with a TT allelic variant (at the SNP most adjacent to the QTL peak; UNC20471277; where T refers to the nucleic acid Thymine) mostly congregate at the higher end of the BV/TV and Tb.N values (Mean BV/TV = 17%); lines with a CC variant (where C refers to the nucleic acid Cytosine) are at the lower end (mean BV/TV = 10%); and those with a CT variant are at the intermediate range (Fig. 5). Largely, the more the trait examined is distantly correlated with BV/TV, the less differentiated the CC and TT variants are, at the SNP

Table 2 Positions of QTLs associated with trabecular and cortical traits

						Simulation					
						50% CI (Mb)		90% CI (Mb)		95% CI (Mb)	
QTL	Trait	Chr	logP	99th % thresh.	H^2_r	Position	Width	Position	Width	Position	Width
Trl7	BV/TV	11	7.60	4.90	0.69	116.6-116.7	0.12	113.6-118.1	4.50	112.1-118.3	6.40
Trl7	Tb.N	11	6.80	4.84	0.71	116.6-116.87	0.29	114.2-118.35	4.15	112.41-118.68	6.27
Trl8	Tb.Th	4	8.00	4.50	0.61	117.2-117.58.	0.32	113.05-125.54	12.49	110.87-126.52	15.65
Trl9	Tb.Sp	5	9.40	6.01	0.78	105.78-106.14	0.35	101.6-109.11	7.54	99.8-110.39	10.62
Crl1	Ct.Th	4	8.20	4.80	0.80	9.29-9.72	0.43	4.0-11.7	7.70	3.4-11.8	8.49
Crl2	vBMD	3	9.80	4.93	0.86	97.2-97.4	0.20	94.4-103.1	8.50	93.22-104.3	10.80

Chr = chromosome; logP = negative 10-base logarithm of P value; Sig = genome-wide significance level; 99th % threshold logP = threshold used to define cut-off for QTL peaks (Fig. 4); H_r^2 = regional heritability (the proprtion to which the locus explains the phenotypic variability). Positions and widths of the simulation-based 50, 90, and 95% CIs are given.

UNC20471277. This is accentuated in vBMD where there is a weak correlation with BV/TV (Table S1) and leveled CC and TT groups (*P* value = 0.8 Welch's two sample t-test).

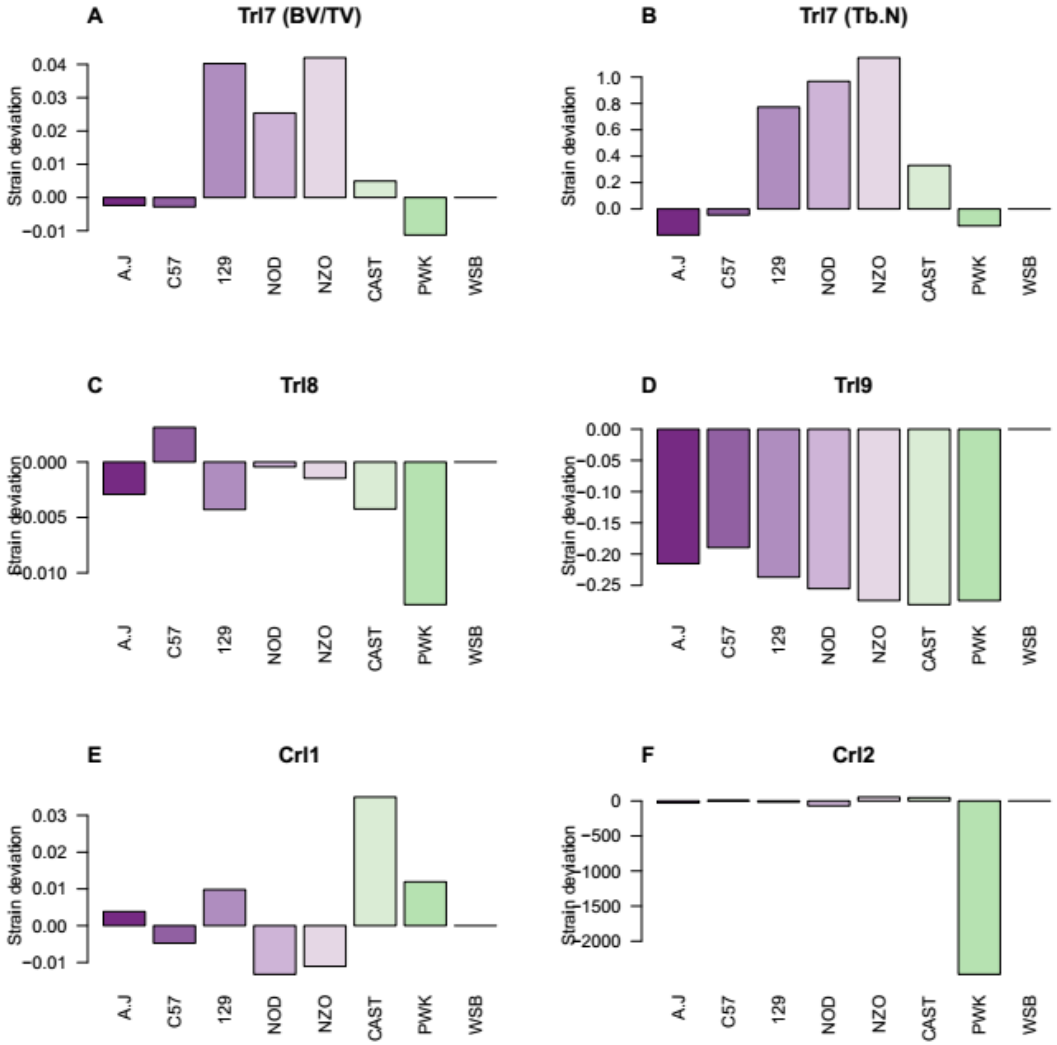

Figure 4 Ancestral effects relative to WSB. Y axis is the strain deviation relative to WSB, x axis is the different strains of the eight CC founders. **(A)** to **(F)**: *Trl7* to *Trl9*, *Crl1*, and *Crl2*, respectively.

Candidate genes identified by merge analysis and publicly available data

We proceeded to refine the haplotype association analysis by merge analysis. This technique uses the catalogue of variants segregating in the eight CC founders in order to impute the genotype dosage of each SNP in each CC line, based on the haplotype reconstruction used for haplotype association. Candidate causal variants, if they exist, would be expected to be more significant (have higher logP values) than the haplotype-based test in the flanking region. We found that *Trl*7 had the highest density of polymorphisms (grey and crimson dots) with merge-logP values above the haplotype logPs (continuous black line), while *Trl*8 and *Crl*2 had very few. The two latter loci congregated more upstream, in accordance with the left-skewness of their respective CI simulations (Fig. S2).

To strengthen the criteria that classifies potential putative candidate gene as true positives, we analyzed RNA-seq datasets of osteoclasts (Fig. S3) and osteocytes (Fig. S4) made publicly available by Kim *et al* (Kim et al. 2016) (Gene Expression Omnibus accession number GSE72846). and St John *et al* (St. John et al. 2014) (Gene Expression Omnibus accession number GSE54784). We focused on local maximas that span ~0.5 Mb in and around the peaks suggested by the merge analysis, for each QTL. From the raw count reads we learnt that *Trl7* had the strongest gene expression differential; e.g *Mxra7* in the osteocyte was expressed to a negligible degree (Fig. S3A), it had a strong presence in osteocytes (Fig. S4A), whereas the genes of the other loci had much less prominent differences.

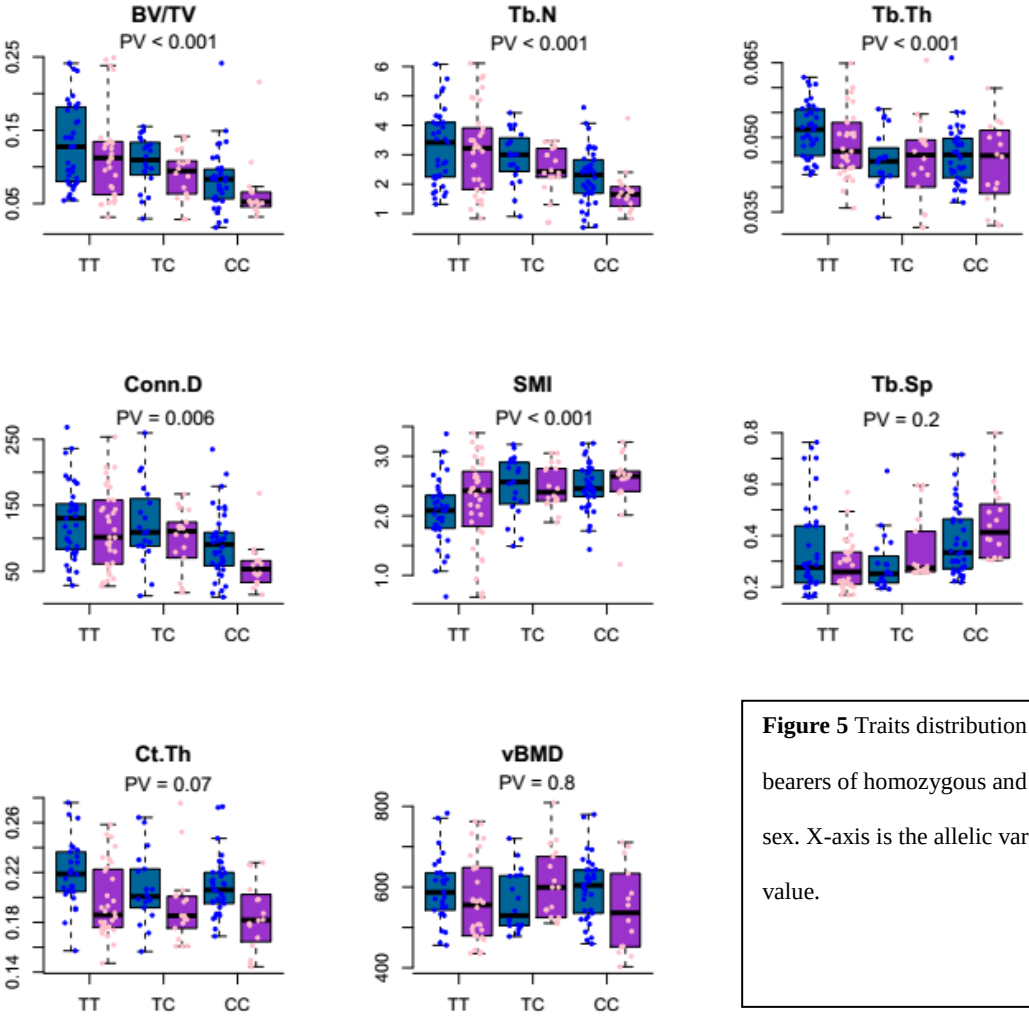

Figure 5 Traits distribution at the marker UNC20471277 across bearers of homozygous and heterozygous alleles, separated by sex. X-axis is the allelic variation at the marker, y-axis is the trait value.

The next layer of information that helped to distill the putative candidate genes list extracted by surveying the literature for (*i*) genes validated experimentally as related to bone; (*ii*) genes validated experimentally as related to bone-related tissues (tendon, cartilage, blood, muscle, etc. in decreasing order of relatedness); (*iii*) genes validated experimentally related to first degree bone-related pathways; and (*iv*) genes (and/or their products) validated experimentally as related to bone-related genes (and/or their products).

By calculating the relative density of merge logP values which are considerably higher than the haplotype merge logPs -and above the 99th percentile threshold for each scan - at intervals defined by each gene within the QTLs (in meaningful regions; usually between the 50th and 90th CI percentile) we devised a

gene ranking scale. This aided us in singling out putative candidate genes; Table S4 contains an exhaustive list of all genes under our loci: bright blue, blue and bright red hues indicate 95, 90, and 50% CI, respectively. For example, while the proportion of merge analysis SNPs for BV/TV and Tb.N with logPs greater than that of the haplotype scan is 1.4% at the genome-wide scale (as well as at the region spanning the 95% CI, between ~112 – 118 Mb), it is 9.4% and ranked 5/36 (for BV/TV) or 14.07% and ranked 3/36 (for Tb.N) at the region in which the gene *Rhbdf2* is situated (~116.5 – 116.6 Mb) (See Table S4 and further discussion below); we thus searched existing reports for *Rhbdf2* possible role in bone biology to evaluate its candidacy.

To account for the data-mining (RNA-seq and literature survey) yield as well, we weighted these data on a comparable scale, and re-sorted the genes accordingly; for example, looking at the 3 genes with the highest merge analysis score in *Trl7*, *Ube2o* had an *osteoclast* RNA-seq score of $S_{RNA\text{-}seq1} = .8$ ($S_{RNA\text{-}seq} = 1 - \frac{r}{n}$; where r is the local gene rank, n is the total number of genes at the locus where if n>10 then n=10), *osteocyte* RNA-seq score of $S_{RNA\text{-}seq2} = .8$, and a literature score of $l = 4$ where l is an integer that reflects the number and relatedness of literature mentions, based on the abovementioned categorization: (*i*) (= 4) to (*iv*) (= 1), and thus a cumulative *Msl* (**m**erge, **s**equencing, and **l**iterature) score of $Msl_{Ube2o} = merge + S_{RNA\text{-}seq1} + S_{RNA\text{-}seq2} + l = 11.1 + .8 + .8 + 3 = 14.62$; while *Aanat* scored $Cum_{Aanat} = 15.4\ 0 + 0 + 0 = 15.4$ and *Rhdbf2* scored $Cum_{Rhbdf2} = 14.07 + .9 + .7 + (2*2 + 3) = 22.67$.

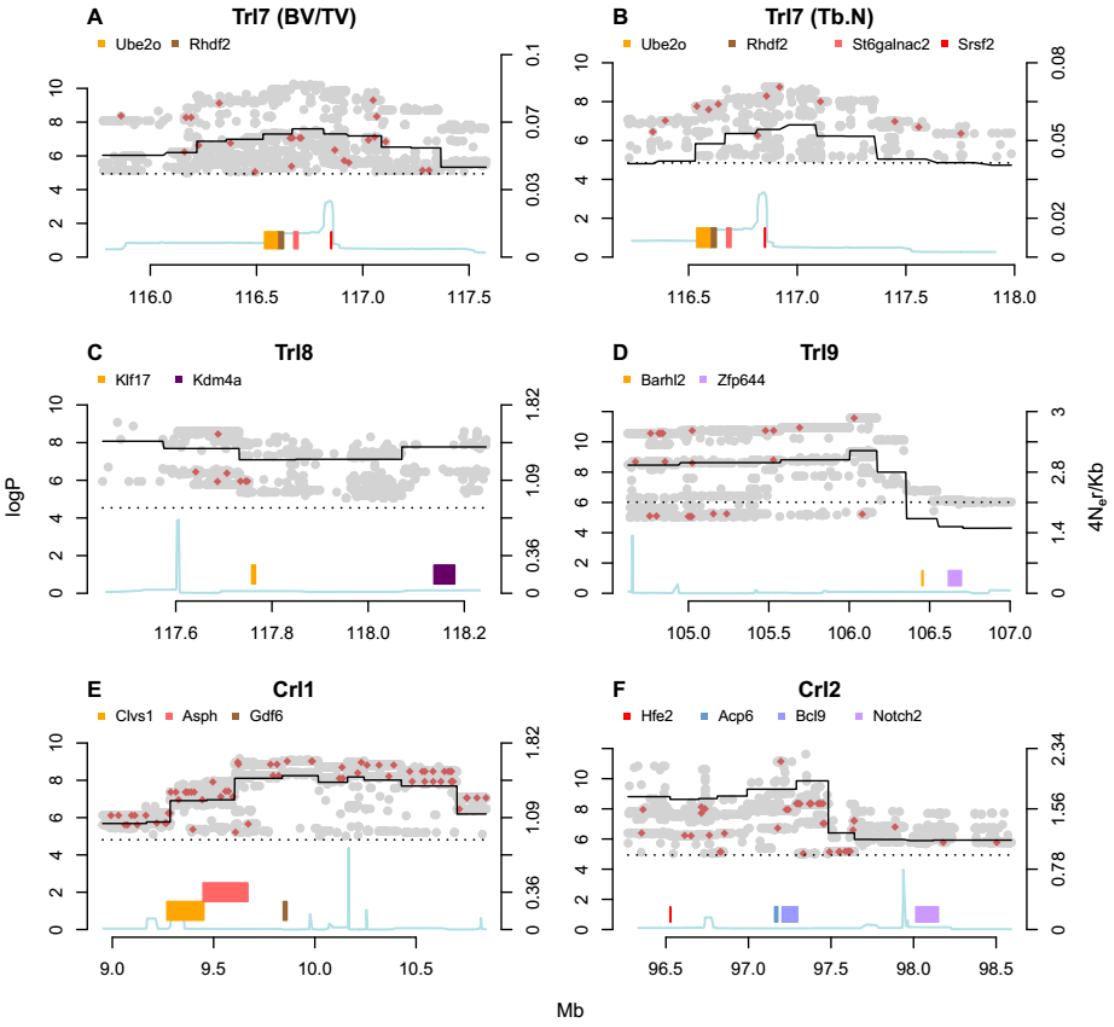

Figure 6 Merge analysis. Readings below logP = 4 are elided for brevity. X axis is the position on the genome in Mb; y left axis is the logP score; y right axis is the recombination rate scale; colored bars are genes (note that only strong putative candidate genes are shown.); cyan line is the recombination rate; black continues line is the haplotype test's peak; dashed line is the 99% permutation threshold. **(A)** to **(F)**: Trl7 of BV/TV, Trl7 of Tb.N, Trl8 of Tb.Th, Trl9 of Tb.Sp, Crl1 of Ct.Th, and Crl2 of vBMD, respectively.

The information our analytical pipeline (the haplotype scans, permutation-based thresholds, FDR, CI simulations, merge analyses, and gene ranking scales) disclosed, converged with that curated from public resources, enabled us to shortlist the genes most plausible to be causal at the QTLs. Because BV/TV is a predominant parameter in bone biology, we first focused on *Trl*7. Of note, *Ube2o* (which is situated at the 90% CI) had a high cummulative score (Cum_{Ube2o} = 15.62) and its role in bone biology is inferred by its link to the SMAD-BMP pathways (Zhang et al. 2013). In the 50th CI percentile, we could not find published reports linking any of the genes to bone microarchitecture. However, because *Rhbdf2* had a merge strength of 14% (the 3rd strongest at the QTL and 2nd at the 50% CI); a local maxima at the RNA-seq of the osteoclasts; was located near the haplotype mapping peak; and is implicated in inflammatory pathways which are known to inter-relate (van der Kraan and

Davidson 2015; Issuree et al. 2013), it was picked for validation. The comprehensive list of the genes under the 50, 90, and 95% CI of the QTL, is supplied in table S4. In particular, the genes under the QTLs most probable as putative functional candidates are *Ube2o* and *Rhbdf2* for *Trl*7; *Klf17* and *Kdm4a* for *Trl*8; *Barhl2* and *Zfp644* for *Trl*9; *Asph* and *Gdf6* for *Crl*1; and *Hfe2*, *Acp6*, *Bcl9*, and *Notch2* for *Crl*2.

Bones of Rhbdf2 knock-out mice significantly differ from their wild-type counterparts

Among the two genes likely to determine the association between the genomic region *Trl*7 and the trabecular trait, we phenotyped *Rhbdf2* knockout (KO) animals, due to its high *Msl* score (see above) Femora of male mice (n=14) null at *Rhbdf2* (on a B6 background) were collected, on which we measured the same morphometric traits as above, including BV/TV, Tb.N, Tb.Th, SMI, Tb.SP, Ct.Th, and vBMD. These were compared to their wild-type (WT) counterparts (n=13), after adjusting for batch, age and weight.

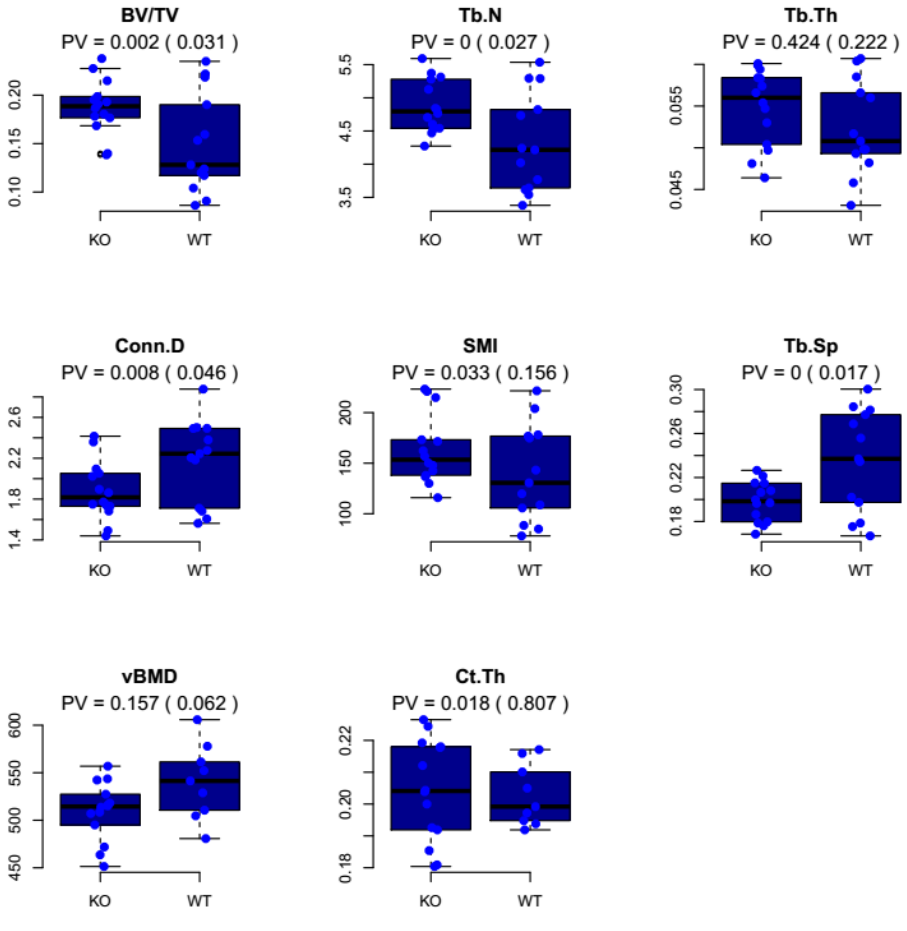

Figure 7 *Rhbdf2* knockout versus wildtype for each of the studied traits. Left is KO, right is WT. PV is the confounder-adjusted P value. The unadjusted P value is in brackets. PV = 0 means PV < 0.001.

Strikingly, we found that *Rhbdf2*$^{-/-}$ mice had a significant bone phenotype. In line with our GWAS data, *Rhbdf2*$^{-/-}$ mice displayed a highly significant increase in BV/TV and Tb.N (Fig. 7, 8). As expected, *Rhbdf2* KO also affected other microstructural parameters, partly due to the high correlation between the trabecular traits. After adjusting for confounders, we observed a significant difference between KO and WT animals in Tb.Sp (P value < 0.001; uncorrected P value = 0.017), SMI (P value = 0.03; uncorrected P value = 0.156) and Conn.D (P value = 0.008; uncorrected P value = 0.046). Tb.Th and vBMD were not affected by the knockout. The cortical compartment also did not display a haplotype peak at the vicinity of *Trl7* in the CC animals. However, after adjusting for confounders, we observed a significant difference in Ct.Th between KO and WT bones (P value = 0. 01), suggesting that the role of *Rhbdf2* is not limited to the trabecular compartment.

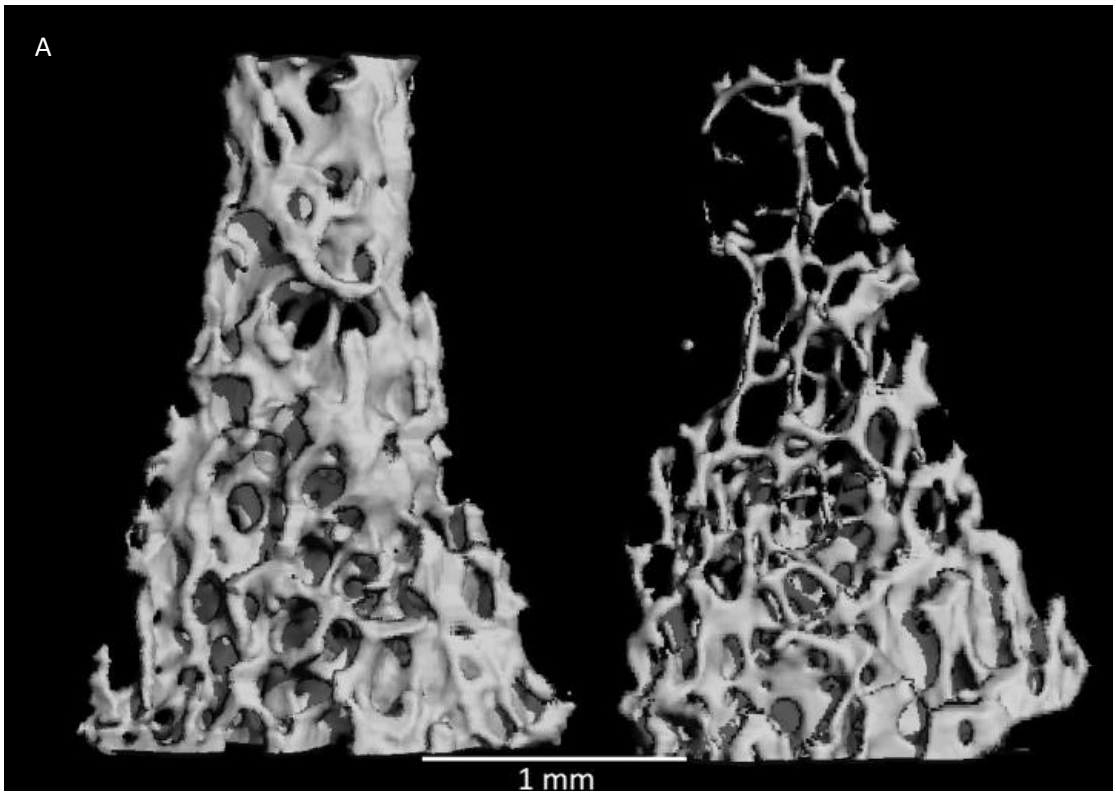

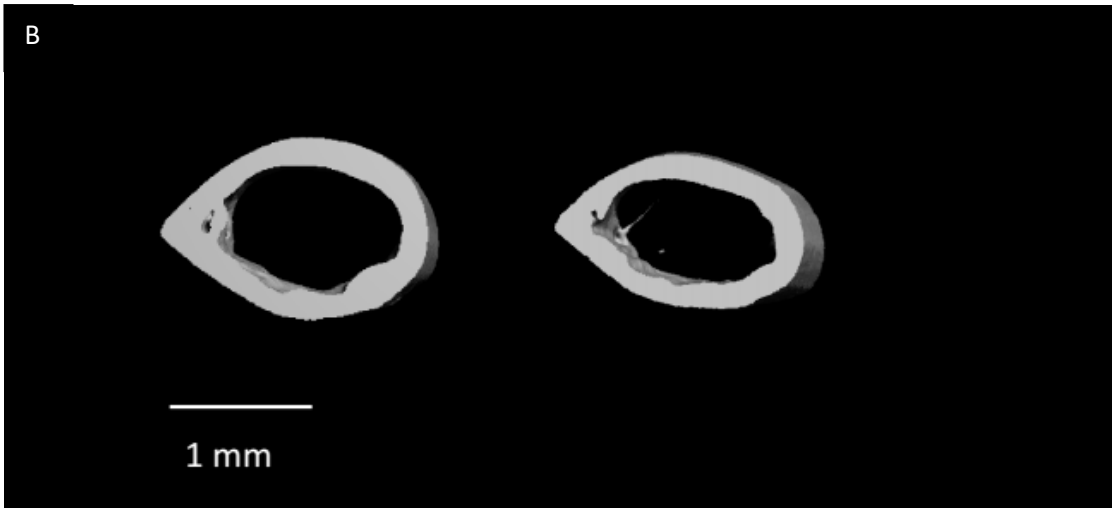

Figure 8 uCT images of three-dimensional representative cortical and trabecular bones reconstructions for *Rhbdf2* knockout and wildtype. Left: KO, right: WT. **(A)** Trabecular bone. **(B)** Cortical bone

Discussion

Genetic reference population (GRP) are very efficient for the study of complex traits and biological systems, because (i) genotyping is only required once ("genotype once, phenotype many times", see below), and (ii) replicate individuals with the same genotype can be generated at will allowing for optimal experimental designs (Broman 2005).

Here we characterize several key microstructural properties of the mouse femoral bone to assess the extent to which they are heritable; to what environmental perturbations they are prone; and to identify candidate genes by which they are controlled. By combining various statistical and high-throughput sequencing analyses together with literature data mining, we were able to shortlist putative candidate genes for 6 of the 8 examined phenotypes. We confirm one candidate gene, *Rhbdf2,* using a knockout model. This article is the second to present the results of an ongoing quest to delineate the genetic determinants that govern microstructural bone traits.

Here we included two additional key trabecular (SMI and Tb.Sp) and cortical (vBMD and Tb.Th) traits. While the heritability rates assessed here - determined to be over 60% for all traits - confirmed our previous findings, the degree to which sex explains the phenotypic variation was very subtle, and appeared only for the cortical traits; this discrepancy may be due to the specific cohort composition used in this study (Table S3), which includes a sex bias due to smaller number of females than males. We found a total of five QTLs in six traits; BV/TV and Tb.N shared one QTL, and Tb.Th, Tb.Sp, vBMD, and Ct.Th yielded one each. Importantly, although bone microarchitecture factors are complex traits, our analyses highlighted no more than two loci for each trait; it is likely that analyzing a larger number of CC lines would result in the identification of further loci.

Our analyses yielded three QTLs for the trabecular traits and 2 QTLs for the cortical traits. These are referred to as *Trl*7-9, and *Crl*1-2, respectively. *Trl*7 includes *Ube2o* (Ubiquitin Conjugating Enzyme E2 O), which encodes an enzyme that is an important interactant of SMAD6; Ube2o monoubiquitinates SMAD6, and thereby facilitates the latter to bind BMP 1 receptors (Zhang et al. 2013). The signal transduction of BMP 1 is in turn limited (Horiki et al. 2004; Estrada et al. 2011), and endochondral bone formation, instead of ossification, is favored. Importantly, 4 week-old SMAD6-overexpressed mice have significantly lower humeral and vertebral BV/TV ratios than their controls (Horiki et al. 2004). In close proximity to this gene is *Rhbdf2* (Rhomboid 5 Homolog 2; elaborated below) which is not yet supported by peer-reviewed reports as bearing a relation to bone, but its nearness to the peak of *Trl*7, density of associated merge-logPs relative to other T*rl7* genes, local osteoclast RNA-seq peak, canonical role in secretion of TNFα (tumor necrosis factor a) and regulation of CSF1R (macrophage stimulating factor 1 receptor; macroohages being

the progenitors of osteocalsts (Udagawa et al. 1990)) ; (Siggs et al. 2012; Adrain et al. 2012a; McIlwain et al. 2012) (and indeed involvement in inflammatory arthritis (Issuree et al. 2013)) made it a probable candidate gene to run validation assays on.

At *Trl*8, *Klf17*, *Kdm4a*, and *Dmap1* are likely putative candidate genes. Since *Klf17* (Kruppel-Like Factor 17) is part of a network that includes BMPs (Kotkamp et al. 2014) it is more likely than a nearby gene, *St3gal3* (ST3 Beta-Galactoside Alpha-2,3-Sialyltransferase 3), to affect bone traits, although the latter has a greater merge strength. *Kdm4a* (Lysine Demethylase 4A) encodes a histone demethylase that promotes the differentiation of embryonal stem cells (ESCs) to an endothelial fate (Wu et al. 2015); endothelial cells are implied in regulation of bone formation (Collin-Osdoby 1994). *Dmap1* (DNA Methyltransferase 1 Associated Protein) which encodes a DNA-methyl transferase known to regulate obesity complications, and is differentially methylated in women with polycystic ovary syndrome (Kokosar et al. 2016; Kamei et al. 2010) had the highest meaningful merge density, and it might epigenetically regulate bone formation as well. *Trl*9 includes two genes of interest to bone biology: *Barhl2* and *Zfp644*. By interacting with caspase3, which is essential for ossification (Miura et al. 2004), *Barhl2* (BarH Like Homeobox 2) can inhibit b-catenin activation (Juraver-Geslin et al. 2011), and regulate the expression of chordin, a BMP signaling-detrimental protein (Larraín et al. 2000). *Zfp644* (Zinc Finger Protein 644), which encodes a transcription repressor zinc-finger protein, is upregulated in eight week-old ovariectomized mice following treatment with estradiol (Davis et al. 2008), a steroidal sex hormone associated with reduced bone loss (Kameda et al. 1997). To support the candidacy of *Zfp644* a marked difference in Tb.Sp between the sexes is anticipated; as expressing more estrogen, females are expected to display denser trabecular network captured as lower Tb.Sp. Even if we

did not find a sex effect for any of the traits excluding Ct.Th, females had a slightly higher mean Tb.Sp, we cannot rule out the possibility that *Trl*9 reflects a differential estrogen effect in the sexes. Further support for the candidacy of *Barhl2* and *Zfp644* is given by the role of *Barhl2* in the development of amacrine cells (Ding et al. 2009; Mo et al. 2004) and the association of *Zfp644* with myopia (Shi et al. 2011), a condition speculated to propagate from amacrine cell signaling (Chen et al. 2006); interestingly myopia was linked to reduced postnatal bone mineral content in humans (Pohlandt 1994) and decreased expression of BMP 2 and 5 in guinea pigs (Wang et al. 2015).

The first of two cortical loci, *Crl*1 contains as likely candidates the genes *Asph* and *Gdf6*. *Asph* (Aspartate Beta-Hydroxylase) encodes a protein that has a role in regulating calcium homeostasis, which may affect bone metabolism (Pruitt et al. 2014). *Gdf6* (Growth Differentiation Factor 6) is bone morphogenetic protein 13: mice with mutated *Gdf6* exhibit deformed bone formation in various skeletal sites; it is among the earliest known markers of limb joint formation (Chang et al. 1994), expressed in joints of ankle and knee. In *Gdf6* homozygous mutant mice a fusion occurs at the joints between bones early at the segmentation stage (Settle et al. 2003). For *Crl*2 we found *Hfe2*, *Bcl9*, *Notch2*, and *Prkab2* as potential candidate genes. *Hfe2* (Hemochromatosis Type 2 (Juvenile)) encodes the BMP co-receptor hemojuvelin which is expressed in skeletal muscles (Verga Falzacappa et al. 2008) and responsible for juvenile hemochromatosis that depletes sex hormones and leads to osteoporosis (Angelopoulos et al. 2006). *Bcl9* (B-Cell CLL/Lymphoma 9), the mammalian ortholog of the gene *Legless*, encodes a protein essential to the Wnt/beta-catenin signaling which is important for bone metabolism (Baron and Kneissel 2013), without which the nuclear localization of beta-catenin and myocyte differentiation are

compromised (Brack et al. 2009). Of note, there are mutual effects between bone and muscle, and accumulating evidence suggest many genes show pleiotrpism with respect to muscle strength and bone parameters (Karasik and Kiel 2008). *Notch2* encodes a member of the notch protein family, which influence both osteoblasts and osteoclasts (Bai et al. 2008); specifically, *Notch2* is associated with the rare Hajdu-Cheney syndrome, that includes severe osteoporosis as one of its main symptoms (Regan and Long 2013; Canalis and Zanotti 2014). For this gene, we did not find any significant merge logPs included within its limits, but *Sec22b*, an adjacent gene, had the strongest merge logP marks in this locus but no documented link to bone biology. The third-strong gene in terms of merge values was *Prkab2* (Protein Kinase AMP-Activated Non-Catalytic Subunit Beta 2). It encodes an enzyme which is the regulatory subunit of mitogen-activated protein kinase (AMPK). AMPK widely affects bone metabolism [36].

Based on its closeness to the *Tlr7* peak (within the 50% CI), the existing literature and its merge strength, we identified *Rhbdf2* as a likely causal gene associated with BV/TV and Tb.N. We therefore analyzed the bone phenotype of *Rhbdf2*$^{-/-}$ mice, to validate the role of this gene in the modeling of the femoral cortex and trabeculae. The KO affected all the trabecular traits examined with Ct.Th and especially prominent in BV/TV, Tb.N, and Tb.Sp. While the effects in BV/TV and Tb.N were in line with the haplotype mapping, the *Rhbdf2* locus did not appear in any of the other traits. This however is expected, because the genetic architecture of the working cohort is such that the assumed contributing variant of *Rhbdf2* is diluted and compensated, resulting in a QTL detected only for the most affected traits. Noticeably, Tb.Sp differed greatly between the *Rhbdf2*$^{-/-}$ and control mice but did not show up at the haplotype mapping; This might be due to (i) the great diversity of the

wild-type mice in Tb.Sp, and/or (ii) the need for complete knockout rather than a mere SNP to detect significant changes in Tb.Sp, and/or (iii) the SNPs giving rise to *Trl*7 are functioning variants, with differential behavior affecting only BV/TV and Tb.N. A similar interpretation may be attempted for the cortical phenotype of the *Rhbdf2*$^{-/-}$ mice. Importantly, the significant QTL peak we found in our GWAS for BV/TV and Tb.N revealed a gene that has an important skeletal function in both the trabecular and cortical bone compartments. .

The *Rhbdf2* gene encodes the iRhom2 protein, a polytopic membrane protein that is a catalytically inactive member of the superfamily related to rhomboid intramembrane serine proteases (Lemberg and Freeman 2007). iRhom2 is necessary in macrophages for the maturation and release of the inflammatory cytokine TNFa: it acts in the trafficking of TACE, the protease that releases active TNFa from its membrane tethered precursor (Adrain et al. 2012b; McIlwain et al. 2012). iRhom2 is also implicated in EGF-family growth factor signaling (Siggs et al. 2014; Hosur et al. 2014; Li et al. 2015). With a recent report of its role in trafficking of another protein, STING, it appears that iRhom2 may have a wider role in regulating membrane trafficking (Luo et al. 2016).

Further work will be needed to identify the mechanism by which iRhom2 controls bone homeostasis; a possible direction could involve a positive feedback loop that leads to differentiation of macrophages to osteoclasts by iRhom2 that stimulates the secretion of TNF-a by macrophages (Kobayashi et al. 2000; Udagawa et al. 1990) ; hyperactivates EGFR (Yi et al. 2008; Hosur et al. 2014); and regulates CSF1R (Hung et al. 2014; Qing et al. 2016).

In summary, our analyses disclose several putative genes, several of which are newly linked to a role in bone biology. A confirmation of one such gene, *Rhbdf2*, provides the first conclusive evidence for its effects on bone microstructure. This finding prompts future investigations looking into the mechanism of action of *Rhbdf2* and its contribution to osteoporosis in humans.

Materials and Methods (also called Methods or Models)

Mice

Mice aged 10 to 13 weeks (male $n = 103$; female $n = 71$), from 34 different CC lines (average of 5 mice per line) were used in this study. The mice were at inbreeding generations of 11 to 37, which correspond to 80-99.9% genetic homozygosity, respectively. The mice were bred and maintained at the small animal facility of the Sackler Faculty of Medicine, Tel Aviv University (TAU), Israel. They were housed on hardwood chip bedding in open-top cages, with food and distilled water available *ad libitum*, in an identical controlled environment (temperature = 25 ± 2°C; 60% ≤ humidity ≤ 85%) and a 12 hour light/dark cycle. All experiments protocols were approved by the Institutional Animal Care and Use Committee (IACUC M-13-014) at TAU, which follows the NIH/USA animal care and use protocols. The *Rhbdl2* knock out mice and their WT counterparts were bred and maintained at the University of Oxford as approved by licence PPL80/2584 of the UK Home Office.

Specimen collection

Mice were intraperitoneally euthanized with cervical dislocation performed approximately one minute after breathing stops owing to 5% Isoflurane inhalation. The *Rhbdl2* knock out mice and their WT counterparts were euthanised by inhalation

of a rising concentration of carbon dioxide followed by dislocation of the neck. Left femora were harvested and fixed for 24 hours in 4% paraformaldehyde solution, and then stored in 70% ethanol.

μCT evaluation

Whole left femora from each mouse were examined as described previously (Hiram-Bab et al. 2015)by a μCT system (μCT 50, Scanco Medical AG, Switzerland). Briefly, scans were performed at a 10-μm resolution in all three spatial dimensions. The mineralized tissues were differentially segmented by a global thresholding procedure (Rüegsegger et al. 1996). All morphometric parameters were determined by a direct 3D approach (Hildebrand et al. 1999). Parameters analyzed were determined in the metaphyseal trabecular bone, which included trabecular bone volume fraction (BV/TV; %), trabecular thickness (Tb.Th; μm), trabecular number (Tb.N; mm^{-1}), trabecular connectivity density (Conn.D; mm^{-3}), trabecular structure model index (SMI), and trabecular separation (Tb.Sp; mm). Two additional parameters are characteristics of the mid-shaft diaphysis section, and include volumetric bone mineral density (vBMD; $mgHA/cm^3$ [mg Hydroxy-Apatite per cm3]) and cortical thickness (Ct.Th; mm). All parameters are generated according to the Guidelines for assessment of bone microstructure in rodents using micro–computed tomography (Bouxsein et al. 2010).

Genotyping

A representative male mouse from each line was initially genotyped with a high mouse diversity array (MDA), which consists of 620,000 SNPs (Durrant et al., 2011). After about two intervals of 4 generations of inbreeding, all the CC lines were regenotyped by mouse universal genotype array (MUGA, 7,500 markers) and finally

with the MegaMuga (77,800 markers) SNP array to confirm their genotype status (Collaborative Cross Consortium 2012). The founder-based mosaic of each CC line was reconstructed using a hidden Markov model (HMM) in which the hidden states are the founder haplotypes and the observed states are the CC lines, to produce a probability matrix of descent from each founder. This matrix was then pruned to about 11,000 SNPs by averaging across a window of 20 consecutive markers for faster analyses and reduction of genotyping errors (Hall et al. 2012).

Statistical analyses and data aquisition

All statistical analyses were performed with the statistical software R (R core development team 2009), including the package happy.hbrem (Mott et al. 2000).

Heritability and covariate effects. Broad-sense heritability (H^2) was obtained for each trait by fitting the trait (the independent variable) to the CC line label in a linear regression model that incorporates relevant covariates (sex, age, batch, month, season, year, and experimenter). ANOVA test was used to compare a null model (in which all dependent variables are set to 0) with linear models that fit the covariates and the CC line labels to the examined trait. Practically, the difference between the residual sum of squares (RSS; $\sum_1^n(\mu_i - \hat{\mu}_i)^2$) of the covariates model and that of the CC-line labels can be seen as the net genetic contribution to the trait. Thus, this difference divided by that of the covariate model gives an estimation of the heritability. Each covariate was calculated separately, by dividing the RSS difference between the null and full model with that of the null model. Let F_0 be the model that fits the trait to the covariates; F_1 the model that fits the trait to the covariates and the CC line label; and F_{00} the null model. Then, employing ANOVA, heritability is:

$$H^2 = (RSS(F_0) - RSS(F_1)) / RSS(F_{00}).$$

Similarly, the effects for each covariate were computed separately, by fitting each in F_0. The covariate effect is thus:

$$(RSS(F_{00}) - RSS(F_1)) / RSS(F_{00}).$$

H^2n was derived from H^2 according to Atamni *et al* (Atamni et al. 2016).

Haplotype mapping. Each trait was fitted in a multiple linear regression model to the probability matrix of descent from each founder, including sex and age as covariates. The expected trait value from two ancestors, termed the genetic fit, is:

$$\mu_i = \mu + \sum_{s,t} F_{Li}(s,t)(\beta_s + \beta_t) = \mu + \sum_s \sum_t F_{Li}(s,t)\beta_s$$

where μ is a normally distributed trait mean, with sex and age incorporated; $F_{Li}(s,t)$ is the probability of descent from founders *s* and *t*; and $\beta_s + \beta_t$ is the additive effect of founders *s* and *t*. Because $\sum_s \sum_t F_{Li}(s,t) = 2$ for a diploid organism, the maximum likelihood estimates $\hat{\beta}_s$ are not independent. Thus, they are expressed here as differences from the WSB/EiJ founder effect, so that $\hat{\beta}_{WSB} = 0$. Number of members per line was weighted and integrated in the linear model. ANOVA was then used to compare this model with a null model where the founder effects are all set to 0; the resulting *F*-statistic yielded the significance of the genetic model *vs*. the null model and the negative 10-base logarithms of the P values (logP) were recorded.

Permutations of the CC lines between the phenotypes were used to set significance thresholds levels. Founder effects are the estimates derived from the multiple linear regression fit above.

Regional heritability (H_r^2) was hereafter computed by ANOVA as in the broad-sense heritability computation, except that here null linear regression fit was compared with a genetic linear regression fit with the probability matrix of the founder descent at the peak QTL as the explanatory variable.

False discovery rate (FDR) was calculated using the p.adjust function in R, with the method "BH" (Benjamini-Hochberg (Hochberg 2016)).

Confidence intervals. Confidence intervals (CIs) were obtained both by simulations and by the quick method of Li, 2011 (Li 2011). In the simulations, we resampled the residuals of the original linear regression fit at the peak of each QTL and rescanned 100 intervals within 7-10 Mb of the original loci to find the highest logP. Accordingly, following Durrant *et al.* (Durrant et al. 2011a), 1000 QTLs were simulated: if $\hat{t}_i$ is a random permutation of the residuals of fitted genetic model at the QTL peak, and *K* is a marker interval in a neighborhood of 3.5 to 5 Mb of the QTL peak *L*, a set of values for each trait, Z_{iK} is provided by:

$$Z_{iK} = \hat{t}_i \exp(\hat{\mu} + \sum_s X_{Kis}\hat{\beta}_s).$$

Merge analysis

In the merge analysis the eight founder strains are partitioned and merged according to the strain distribution pattern (SDP) of the alleles at the quantitative trait nucleotides (QTN) within a given QTL (formerly obtained by the initial mapping). If

we denote the polymorphism as *p*, then $X_p = 1$ if *s* has allele *a* at *p*, and $X_p = 0$ otherwise (Yalcin et al. 2005). Then, at *p*, the probability of *i* to inherit alleles *a and b* from *s and t, respectively*, within *L* is

$$G_{pi}(a,b) = \sum_{s,t} X_p\,(a,s) X_p(b,t) F_{Li}(s,t).$$

This merges the founder strains by *p*. The expected trait value in the merged strains can now be inferred by

$$\sum_{a,b} G_{pi}\,(a,b)(\beta_a + \beta_b).$$

Because this is a sub-model of the QTL model, it is expected to yield higher logP values due to a reduction in the degrees of freedom. Significance was obtained by comparing the merge model with the QTL model. Individual genes were extracted from the Sanger mouse SNP repository (http://www.sanger.ac.uk/sanger/Mouse_SnpViewer).

Merge strength

We ranked the list of genes under each QTL according to the density of merge logPs associated with them: only genes that had merge logPs above the haplotype mapping reading, and above the threshold, plus logP=1 were included. We then computed the relative density according to the density of a given gene's merge logPs versus the locus' merge logP density. Let *g* be the region encompassed by a gene; *l* the region encompassed by a QTL; and *mp* the merge logP values above the haplotype P values

plus 1. Then $g_i(mp) = 1$ if at SNP *i* there exists a *mp* and 0 otherwise. Similarly $l_i(mp) = 1$ if at SNP *j* there exists a *mp* and 0 otherwise. The merge strength (MS) is therefore:

$$MS\ [\%] = 100 * \frac{\sum_i g_i(mp)}{\sum_j l_j(mp)}\%.$$

RNA-seq data

RNA-seq data from osteoclasts and osteocytes was obtained from gene expression omnibus (GEO) database (accession numbers GSE72846 and GSE54784) and mapped to the mus musculus assembly mm10 using tophat v. 2 (Trapnell et al. 2009). Read counts were then casted on the loci of interest using the R (R Core Team 2015) package GenomicAlignments and raw read counts were taken. For the osteocytes, the data of basal level day 3 was averaged.

Acknowledgments

This study was supported by Tel Aviv University starter funds and by Israel Science Foundation (ISF) grant 1822/12 to YG, by Wellcome Trust grants 085906/Z/08/Z, 075491/Z/04, and 090532/Z/09/Z to RM, core funding by Tel-Aviv University to FI, Wellcome Trust grant 101035/Z/13/Z and the Medical Research Council (programme number U105178780) to MF, and by a fellowship from the Edmond J. Safra Center for Bioinformatics at Tel-Aviv University to RL.

References

Adrain C, Zettl M, Christova Y, Taylor N, Freeman M. 2012a. Tumor Necrosis Factor Signaling Requires iRhom2 to Promote Trafficking and Activation of TACE. *Science (80-)* **335**: 225–228. http://www.ncbi.nlm.nih.gov/pubmed/22246777 (Accessed December 10, 2016).

Adrain C, Zettl M, Christova Y, Taylor N, Freeman M, References A. 2012b. Supporting Online Material for. **225**.

Angelopoulos NG, Goula AK, Papanikolaou G, Tolis G. 2006. Osteoporosis in HFE2 juvenile hemochromatosis. A case report and review of the literature. *Osteoporos Int* **17**: 150–5. http://www.ncbi.nlm.nih.gov/pubmed/15997423 (Accessed May 4, 2016).

Atamni HJA-T, Mott R, Soller M, Iraqi FA. 2016. High-fat-diet induced development of increased fasting glucose levels and impaired response to intraperitoneal glucose challenge in the collaborative cross mouse genetic reference population. *BMC Genet* **17**: 10. http://bmcgenet.biomedcentral.com/articles/10.1186/s12863-015-0321-x (Accessed January 6, 2016).

Bai S, Kopan R, Zou W, Hilton MJ, Ong C, Long F, Ross FP, Teitelbaum SL. 2008. NOTCH1 regulates osteoclastogenesis directly in osteoclast precursors and indirectly via osteoblast lineage cells. *J Biol Chem* **283**: 6509–18. http://www.ncbi.nlm.nih.gov/pubmed/18156632 (Accessed May 5, 2016).

Baron R, Kneissel M. 2013. WNT signaling in bone homeostasis and disease: from human mutations to treatments. *Nat Med* **19**: 179–92. http://dx.doi.org/10.1038/nm.3074 (Accessed February 29, 2016).

Bouxsein ML, Boyd SK, Christiansen BA, Guldberg RE, Jepsen KJ, Müller R. 2010. Guidelines for assessment of bone microstructure in rodents using micro-computed tomography. *J Bone Miner Res* **25**: 1468–86. http://www.ncbi.nlm.nih.gov/pubmed/20533309 (Accessed April 11, 2016).

Brack AS, Murphy-Seiler F, Hanifi J, Deka J, Eyckerman S, Keller C, Aguet M, Rando TA. 2009. BCL9 is an essential component of canonical Wnt signaling that mediates the differentiation of myogenic progenitors during muscle regeneration. *Dev Biol* **335**: 93–105. http://www.pubmedcentral.nih.gov/articlerender.fcgi?artid=3259687&tool=pmcentrez&rendertype=abstract (Accessed May 4, 2016).

Broman KW. 2005. The genomes of recombinant inbred lines. *Genetics* **169**: 1133–46. http://www.pubmedcentral.nih.gov/articlerender.fcgi?artid=1449115&tool=pmcentrez&rendertype=abstract (Accessed February 5, 2014).

Burge R, Dawson-Hughes B, Solomon DH, Wong JB, King A, Tosteson A. 2007. Incidence and economic burden of osteoporosis-related fractures in the United States, 2005-2025. *J Bone Miner Res* **22**: 465–75. http://www.ncbi.nlm.nih.gov/pubmed/17144789 (Accessed June 22, 2015).

Canalis E, Zanotti S. 2014. Hajdu-Cheney syndrome: a review. *Orphanet J Rare Dis* **9**: 200. http://ojrd.biomedcentral.com/articles/10.1186/s13023-014-0200-y (Accessed May 4, 2016).

Center JR, Nguyen T V, Schneider D, Sambrook PN, Eisman JA. 1999. Mortality after all major types of osteoporotic fracture in men and women: an observational study. *Lancet (London, England)* **353**: 878–82.

http://www.ncbi.nlm.nih.gov/pubmed/10093980 (Accessed June 20, 2016).

Chang SC, Hoang B, Thomas JT, Vukicevic S, Luyten FP, Ryba NJ, Kozak CA, Reddi AH, Moos M. 1994. Cartilage-derived morphogenetic proteins. New members of the transforming growth factor-beta superfamily predominantly expressed in long bones during human embryonic development. *J Biol Chem* **269**: 28227–34. http://www.ncbi.nlm.nih.gov/pubmed/7961761 (Accessed February 16, 2016).

Chen JC, Brown B, Schmid KL. 2006. Evaluation of inner retinal function in myopia using oscillatory potentials of the multifocal electroretinogram. *Vision Res* **46**: 4096–103. http://www.sciencedirect.com/science/article/pii/S0042698906003567 (Accessed May 3, 2016).

Churchill G a, Airey DC, Allayee H, Angel JM, Attie AD, Beatty J, Beavis WD, Belknap JK, Bennett B, Berrettini W, et al. 2004. The Collaborative Cross, a community resource for the genetic analysis of complex traits. *Nat Genet* **36**: 1133–7. http://www.ncbi.nlm.nih.gov/pubmed/15514660.

Collaborative Cross Consortium. 2012. The genome architecture of the Collaborative Cross mouse genetic reference population. *Genetics* **190**: 389–401. http://www.genetics.org/content/190/2/389.full (Accessed February 19, 2014).

Collin-Osdoby P. 1994. Role of vascular endothelial cells in bone biology. *J Cell Biochem* **55**: 304–9. http://www.ncbi.nlm.nih.gov/pubmed/7962161 (Accessed February 15, 2016).

Davis AM, Mao J, Naz B, Kohl JA, Rosenfeld CS. 2008. Comparative effects of estradiol, methyl-piperidino-pyrazole, raloxifene, and ICI 182 780 on gene expression in the murine uterus. *J Mol Endocrinol* **41**: 205–17. http://jme.endocrinology-journals.org/content/41/4/205.abstract (Accessed May 3, 2016).

Dhanwal DK, Dennison EM, Harvey NC, Cooper C. 2011. Epidemiology of hip fracture: Worldwide geographic variation. *Indian J Orthop* **45**: 15–22. http://www.pubmedcentral.nih.gov/articlerender.fcgi?artid=3004072&tool=pmcentrez&rendertype=abstract (Accessed May 13, 2015).

Ding Q, Chen H, Xie X, Libby RT, Tian N, Gan L. 2009. BARHL2 differentially regulates the development of retinal amacrine and ganglion neurons. *J Neurosci* **29**: 3992–4003. http://www.pubmedcentral.nih.gov/articlerender.fcgi?artid=2756297&tool=pmcentrez&rendertype=abstract (Accessed May 3, 2016).

Durrant C, Tayem H, Yalcin B, Cleak J, Goodstadt L, de Villena FP-M, Mott R, Iraqi F a. 2011a. Collaborative Cross mice and their power to map host susceptibility to Aspergillus fumigatus infection. *Genome Res* **21**: 1239–48. http://www.pubmedcentral.nih.gov/articlerender.fcgi?artid=3149491&tool=pmcentrez&rendertype=abstract (Accessed February 19, 2014).

Durrant C, Tayem H, Yalcin B, Cleak J, Goodstadt L, Villena FP De, Mott R, Iraqi FA. 2011b. Collaborative Cross mice and their power to map host susceptibility to Aspergillus fumigatus infection Collaborative Cross mice and their power to map host susceptibility to Aspergillus fumigatus infection.

Estrada K, Styrkarsdottir U, Evangelou E, Hsu Y-H, Duncan EL, Ntzani EE, Oei L, Albagha OME, Amin N, Kemp JP, et al. 2012. Genome-wide meta-analysis identifies 56 bone mineral density loci and reveals 14 loci associated with risk of

fracture. *Nat Genet* **44**: 491–501. http://www.pubmedcentral.nih.gov/articlerender.fcgi?artid=3338864&tool=pmcentrez&rendertype=abstract (Accessed February 19, 2014).

Estrada KD, Retting KN, Chin AM, Lyons KM. 2011. Smad6 is essential to limit BMP signaling during cartilage development. *J Bone Miner Res* **26**: 2498–510. http://www.pubmedcentral.nih.gov/articlerender.fcgi?artid=3183270&tool=pmcentrez&rendertype=abstract (Accessed February 15, 2016).

Hall M, Manship G, Morahan G, Pettit K, Scholten J, Tweedie K, Wallace A, Weerasekera L, Aylor DL, Baric RS, et al. 2012. The genome architecture of the Collaborative Cross mouse genetic reference population. *Genetics* **190**: 389–401. http://www.pubmedcentral.nih.gov/articlerender.fcgi?artid=3276630&tool=pmcentrez&rendertype=abstract (Accessed February 19, 2014).

Hildebrand T, Laib A, Müller R, Dequeker J, Rüegsegger P. 1999. Direct three-dimensional morphometric analysis of human cancellous bone: microstructural data from spine, femur, iliac crest, and calcaneus. *J Bone Miner Res* **14**: 1167–74. http://www.ncbi.nlm.nih.gov/pubmed/10404017 (Accessed May 13, 2015).

Hiram-Bab S, Liron T, Deshet-Unger N, Mittelman M, Gassmann M, Rauner M, Franke K, Wielockx B, Neumann D, Gabet Y. 2015. Erythropoietin directly stimulates osteoclast precursors and induces bone loss. *FASEB J* **29**: 1890–900. http://www.ncbi.nlm.nih.gov/pubmed/25630969 (Accessed July 22, 2015).

Hochberg Y. 2016. Controlling the False Discovery Rate : A Practical and Powerful Approach to Multiple Testing Author (s): Yoav Benjamini and Yosef Hochberg Source : Journal of the Royal Statistical Society . Series B (Methodological), Vol . 57 , No . 1 (1995), Publi. **57**: 289–300.

Horiki M, Imamura T, Okamoto M, Hayashi M, Murai J, Myoui A, Ochi T, Miyazono K, Yoshikawa H, Tsumaki N. 2004. Smad6/Smurf1 overexpression in cartilage delays chondrocyte hypertrophy and causes dwarfism with osteopenia. *J Cell Biol* **165**: 433–45. http://www.pubmedcentral.nih.gov/articlerender.fcgi?artid=2172180&tool=pmcentrez&rendertype=abstract (Accessed January 20, 2016).

Hosur V, Johnson KR, Burzenski LM, Stearns TM, Maser RS, Shultz LD. 2014. Rhbdf2 mutations increase its protein stability and drive EGFR hyperactivation through enhanced secretion of amphiregulin. *Proc Natl Acad Sci* **111**: E2200–E2209. http://www.ncbi.nlm.nih.gov/pubmed/24825892 (Accessed December 10, 2016).

Hsu Y-H, Kiel DP. 2012. Clinical review: Genome-wide association studies of skeletal phenotypes: what we have learned and where we are headed. *J Clin Endocrinol Metab* **97**: E1958-77. http://www.pubmedcentral.nih.gov/articlerender.fcgi?artid=3674343&tool=pmcentrez&rendertype=abstract (Accessed March 24, 2014).

Hung JY, Horn D, Woodruff K, Prihoda T, LeSaux C, Peters J, Tio F, Abboud-Werner SL. 2014. Colony-stimulating factor 1 potentiates lung cancer bone metastasis. *Lab Investig* **94**: 371–381. http://www.ncbi.nlm.nih.gov/pubmed/24468794 (Accessed December 10, 2016).

Iraqi F a, Athamni H, Dorman A, Salymah Y, Tomlinson I, Nashif A, Shusterman A, Weiss E, Houri-Haddad Y, Mott R, et al. 2014. Heritability and coefficient of genetic variation analyses of phenotypic traits provide strong basis for high-resolution QTL mapping in the Collaborative Cross mouse genetic reference population. *Mamm Genome* **25**: 109–19. http://www.ncbi.nlm.nih.gov/pubmed/24445421 (Accessed December 25, 2014).

Issuree PDA, Maretzky T, McIlwain DR, Monette S, Qing X, Lang PA, Swendeman SL, Park-Min K-H, Binder N, Kalliolias GD, et al. 2013. iRHOM2 is a critical pathogenic mediator of inflammatory arthritis. *J Clin Invest* **123**: 928–32. http://www.ncbi.nlm.nih.gov/pubmed/23348744 (Accessed December 10, 2016).

Jeyabalan J, Shah M, Viollet B, Chenu C. 2012. AMP-activated protein kinase pathway and bone metabolism. *J Endocrinol* **212**: 277–90. http://www.ncbi.nlm.nih.gov/pubmed/21903861 (Accessed November 15, 2015).

Jovanovich A, Bùzková P, Chonchol M, Robbins J, Fink HA, de Boer IH, Kestenbaum B, Katz R, Carbone L, Lee J, et al. 2013. Fibroblast growth factor 23, bone mineral density, and risk of hip fracture among older adults: the cardiovascular health study. *J Clin Endocrinol Metab* **98**: 3323–31. http://www.ncbi.nlm.nih.gov/pubmed/23771921 (Accessed March 24, 2014).

Juraver-Geslin HA, Ausseil JJ, Wassef M, Durand BC. 2011. Barhl2 limits growth of the diencephalic primordium through Caspase3 inhibition of beta-catenin activation. *Proc Natl Acad Sci U S A* **108**: 2288–93. http://www.pubmedcentral.nih.gov/articlerender.fcgi?artid=3038765&tool=pmcentrez&rendertype=abstract (Accessed February 16, 2016).

Kameda T, Mano H, Yuasa T, Mori Y, Miyazawa K, Shiokawa M, Nakamaru Y, Hiroi E, Hiura K, Kameda A, et al. 1997. Estrogen inhibits bone resorption by directly inducing apoptosis of the bone-resorbing osteoclasts. *J Exp Med* **186**: 489–95. http://www.pubmedcentral.nih.gov/articlerender.fcgi?artid=2199029&tool=pmcentrez&rendertype=abstract (Accessed May 3, 2016).

Kamei Y, Suganami T, Ehara T, Kanai S, Hayashi K, Yamamoto Y, Miura S, Ezaki O, Okano M, Ogawa Y. 2010. Increased expression of DNA methyltransferase 3a in obese adipose tissue: studies with transgenic mice. *Obesity (Silver Spring)* **18**: 314–21. http://www.ncbi.nlm.nih.gov/pubmed/19680236 (Accessed June 1, 2016).

Karasik D, Demissie S, Zhou Y, Lu D, Broe KE, Bouxsein ML, Cupples LA, Kiel DP. 2016. Heritability and Genetic Correlations for Bone Microarchitecture: The Framingham Study Families. *J Bone Miner Res*. http://doi.wiley.com/10.1002/jbmr.2915 (Accessed October 24, 2016).

Karasik D, Kiel DP. 2008. Genetics of the musculoskeletal system: a pleiotropic approach. *J Bone Miner Res* **23**: 788–802. http://www.pubmedcentral.nih.gov/articlerender.fcgi?artid=3280426&tool=pmcentrez&rendertype=abstract (Accessed May 19, 2015).

Keane TM, Goodstadt L, Danecek P, White M a, Wong K, Yalcin B, Heger A, Agam A, Slater G, Goodson M, et al. 2011. Mouse genomic variation and its effect on phenotypes and gene regulation. *Nature* **477**: 289–94. http://www.pubmedcentral.nih.gov/articlerender.fcgi?artid=3276836&tool=pmcentrez&rendertype=abstract (Accessed January 20, 2014).

Kim K, Punj V, Kim J-M, Lee S, Ulmer TS, Lu W, Rice JC, An W. 2016. MMP-9 facilitates selective proteolysis of the histone

H3 tail at genes necessary for proficient osteoclastogenesis. *Genes Dev* **30**: 208–19. http://www.ncbi.nlm.nih.gov/pubmed/26744418 (Accessed December 10, 2016).

Kobayashi K, Takahashi N, Jimi E, Udagawa N, Takami M, Kotake S, Nakagawa N, Kinosaki M, Yamaguchi K, Shima N, et al. 2000. Tumor necrosis factor alpha stimulates osteoclast differentiation by a mechanism independent of the ODF/RANKL-RANK interaction. *J Exp Med* **191**: 275–86. http://www.pubmedcentral.nih.gov/articlerender.fcgi?artid=2195746&tool=pmcentrez&rendertype=abstract (Accessed March 4, 2016).

Kokosar M, Benrick A, Perfilyev A, Fornes R, Nilsson E, Maliqueo M, Behre CJ, Sazonova A, Ohlsson C, Ling C, et al. 2016. Epigenetic and Transcriptional Alterations in Human Adipose Tissue of Polycystic Ovary Syndrome. *Sci Rep* **6**: 22883. http://www.pubmedcentral.nih.gov/articlerender.fcgi?artid=4791632&tool=pmcentrez&rendertype=abstract (Accessed June 1, 2016).

Kotkamp K, Mössner R, Allen A, Onichtchouk D, Driever W. 2014. A Pou5f1/Oct4 dependent Klf2a, Klf2b, and Klf17 regulatory sub-network contributes to EVL and ectoderm development during zebrafish embryogenesis. *Dev Biol* **385**: 433–47. http://www.ncbi.nlm.nih.gov/pubmed/24211655 (Accessed February 15, 2016).

Larraín J, Bachiller D, Lu B, Agius E, Piccolo S, De Robertis EM. 2000. BMP-binding modules in chordin: a model for signalling regulation in the extracellular space. *Development* **127**: 821–30. http://www.pubmedcentral.nih.gov/articlerender.fcgi?artid=2280033&tool=pmcentrez&rendertype=abstract (Accessed February 16, 2016).

Lemberg MK, Freeman M. 2007. Functional and evolutionary implications of enhanced genomic analysis of rhomboid intramembrane proteases. *Genome Res* **17**: 1634–1646. http://www.ncbi.nlm.nih.gov/pubmed/17938163 (Accessed December 10, 2016).

Levy R, Mott RF, Iraqi FA, Gabet Y. 2015a. Collaborative cross mice in a genetic association study reveal new candidate genes for bone microarchitecture. *BMC Genomics* **16**: 1013. http://www.biomedcentral.com/1471-2164/16/1013 (Accessed November 27, 2015).

Levy R, Mott RF, Iraqi FA, Gabet Y. 2015b. Collaborative cross mice in a genetic association study reveal new candidate genes for bone microarchitecture. *BMC Genomics* **16**: 1013. http://www.biomedcentral.com/1471-2164/16/1013.

Li H. 2011. A quick method to calculate QTL confidence interval. *J Genet* **90**: 355–60. http://www.ncbi.nlm.nih.gov/pubmed/21869489 (Accessed May 18, 2015).

Li X, Maretzky T, Weskamp G, Monette S, Qing X, Issuree PDA, Crawford HC, McIlwain DR, Mak TW, Salmon JE, et al. 2015. iRhoms 1 and 2 are essential upstream regulators of ADAM17-dependent EGFR signaling. *Proc Natl Acad Sci U S A* **112**: 6080–5. http://www.ncbi.nlm.nih.gov/pubmed/25918388 (Accessed December 10, 2016).

Luo W-W, Li S, Li C, Lian H, Yang Q, Zhong B, Shu H-B. 2016. iRhom2 is essential for innate immunity to DNA viruses by mediating trafficking and stability of the adaptor STING. *Nat Immunol* **17**: 1057–1066. http://www.ncbi.nlm.nih.gov/pubmed/27428826 (Accessed December 10, 2016).

McIlwain DR, Lang PA, Maretzky T, Hamada K, Ohishi K, Maney SK, Berger T, Murthy A, Duncan G, Xu HC, et al. 2012.

iRhom2 Regulation of TACE Controls TNF-Mediated Protection Against Listeria and Responses to LPS. *Science (80-)* **335**: 229–232. http://www.ncbi.nlm.nih.gov/pubmed/22246778 (Accessed December 10, 2016).

Miura M, Chen X-D, Allen MR, Bi Y, Gronthos S, Seo B-M, Lakhani S, Flavell RA, Feng X-H, Robey PG, et al. 2004. A crucial role of caspase-3 in osteogenic differentiation of bone marrow stromal stem cells. *J Clin Invest* **114**: 1704–13. http://www.pubmedcentral.nih.gov/articlerender.fcgi?artid=535063&tool=pmcentrez&rendertype=abstract (Accessed November 16, 2015).

Mizuguchi T, Furuta I, Watanabe Y, Tsukamoto K, Tomita H, Tsujihata M, Ohta T, Kishino T, Matsumoto N, Minakami H, et al. 2004. LRP5, low-density-lipoprotein-receptor-related protein 5, is a determinant for bone mineral density. *J Hum Genet* **49**: 80–6. http://www.ncbi.nlm.nih.gov/pubmed/14727154 (Accessed February 19, 2014).

Mo Z, Li S, Yang X, Xiang M. 2004. Role of the Barhl2 homeobox gene in the specification of glycinergic amacrine cells. *Development* **131**: 1607–18. http://www.ncbi.nlm.nih.gov/pubmed/14998930 (Accessed May 3, 2016).

Mott R, Talbot CJ, Turri MG, Collins a C, Flint J. 2000. A method for fine mapping quantitative trait loci in outbred animal stocks. *Proc Natl Acad Sci U S A* **97**: 12649–54. http://www.pubmedcentral.nih.gov/articlerender.fcgi?artid=18818&tool=pmcentrez&rendertype=abstract.

Paternoster L, Lorentzon M, Lehtimäki T, Eriksson J, Kähönen M, Raitakari O, Laaksonen M, Sievänen H, Viikari J, Lyytikäinen L-P, et al. 2013. Genetic determinants of trabecular and cortical volumetric bone mineral densities and bone microstructure. *PLoS Genet* **9**: e1003247. http://www.pubmedcentral.nih.gov/articlerender.fcgi?artid=3578773&tool=pmcentrez&rendertype=abstract (Accessed February 19, 2014).

Paternoster L, Lorentzon M, Vandenput L, Karlsson MK, Ljunggren O, Kindmark A, Mellstrom D, Kemp JP, Jarett CE, Holly JMP, et al. 2010. Genome-wide association meta-analysis of cortical bone mineral density unravels allelic heterogeneity at the RANKL locus and potential pleiotropic effects on bone. *PLoS Genet* **6**: e1001217. http://www.pubmedcentral.nih.gov/articlerender.fcgi?artid=2987837&tool=pmcentrez&rendertype=abstract (Accessed February 19, 2014).

Pohlandt F. 1994. Hypothesis: myopia of prematurity is caused by postnatal bone mineral deficiency. *Eur J Pediatr* **153**: 234–6. http://www.ncbi.nlm.nih.gov/pubmed/8194552 (Accessed May 3, 2016).

Pruitt KD, Brown GR, Hiatt SM, Thibaud-Nissen F, Astashyn A, Ermolaeva O, Farrell CM, Hart J, Landrum MJ, McGarvey KM, et al. 2014. RefSeq: an update on mammalian reference sequences. *Nucleic Acids Res* **42**: D756-63. http://www.pubmedcentral.nih.gov/articlerender.fcgi?artid=3965018&tool=pmcentrez&rendertype=abstract (Accessed February 16, 2016).

Qing X, D. Rogers L, Mortha A, Lavin Y, Redecha P, Issuree PD, Maretzky T, Merad M, R. McIlwain D, Mak TW, et al. 2016. iRhom2 regulates CSF1R cell surface expression and non-steady state myelopoiesis in mice. *Eur J Immunol* **46**: 2737–2748. http://www.ncbi.nlm.nih.gov/pubmed/27601030 (Accessed December 10, 2016).

Regan J, Long F. 2013. Notch signaling and bone remodeling. *Curr Osteoporos Rep* **11**: 126–9. http://www.pubmedcentral.nih.gov/articlerender.fcgi?artid=3645324&tool=pmcentrez&rendertype=abstract (Accessed

May 4, 2016).

Richards JB, Rivadeneira F, Inouye M, Pastinen TM, Soranzo N, Wilson SG, Andrew T, Falchi M, Gwilliam R, Ahmadi KR, et al. 2008. Bone mineral density, osteoporosis, and osteoporotic fractures: a genome-wide association study. *Lancet* **371**: 1505–12. http://www.pubmedcentral.nih.gov/articlerender.fcgi?artid=2679414&tool=pmcentrez&rendertype=abstract (Accessed January 22, 2014).

Roberts A, Pardo-Manuel de Villena F, Wang W, McMillan L, Threadgill DW. 2007. The polymorphism architecture of mouse genetic resources elucidated using genome-wide resequencing data: implications for QTL discovery and systems genetics. *Mamm Genome* **18**: 473–81. http://www.pubmedcentral.nih.gov/articlerender.fcgi?artid=1998888&tool=pmcentrez&rendertype=abstract (Accessed February 19, 2014).

Rüegsegger P, Koller B, Müller R. 1996. A microtomographic system for the nondestructive evaluation of bone architecture. *Calcif Tissue Int* **58**: 24–29. http://link.springer.com/10.1007/BF02509542 (Accessed May 31, 2015).

Settle SH, Rountree RB, Sinha A, Thacker A, Higgins K, Kingsley DM. 2003. Multiple joint and skeletal patterning defects caused by single and double mutations in the mouse Gdf6 and Gdf5 genes. *Dev Biol* **254**: 116–30. http://www.ncbi.nlm.nih.gov/pubmed/12606286 (Accessed February 16, 2016).

Shi Y, Li Y, Zhang D, Zhang H, Li Y, Lu F, Liu X, He F, Gong B, Cai L, et al. 2011. Exome sequencing identifies ZNF644 mutations in high myopia. *PLoS Genet* **7**: e1002084. http://www.pubmedcentral.nih.gov/articlerender.fcgi?artid=3111487&tool=pmcentrez&rendertype=abstract (Accessed May 3, 2016).

Siggs OM, Grieve A, Xu H, Bambrough P, Christova Y, Freeman M. 2014. Genetic interaction implicates iRhom2 in the regulation of EGF receptor signalling in mice. *Biol Open* **3**.

Siggs OM, Xiao N, Wang Y, Shi H, Tomisato W, Li X, Xia Y, Beutler B. 2012. iRhom2 is required for the secretion of mouse TNFα. *Blood* **119**: 5769–71. http://www.bloodjournal.org/content/119/24/5769.abstract (Accessed February 15, 2016).

St. John HC, Bishop KA, Meyer MB, Benkusky NA, Leng N, Kendziorski C, Bonewald LF, Pike JW. 2014. The Osteoblast to Osteocyte Transition: Epigenetic Changes and Response to the Vitamin D $_3$ Hormone. *Mol Endocrinol* **28**: 1150–1165. http://www.ncbi.nlm.nih.gov/pubmed/24877565 (Accessed December 10, 2016).

Styrkarsdottir U, Halldorsson B V, Gretarsdottir S, Gudbjartsson DF, Walters GB, Ingvarsson T, Jonsdottir T, Saemundsdottir J, Center JR, Nguyen T V, et al. 2008. Multiple genetic loci for bone mineral density and fractures. *N Engl J Med* **358**: 2355–65. http://www.ncbi.nlm.nih.gov/pubmed/18445777.

Styrkarsdottir U, Thorleifsson G, Sulem P, Gudbjartsson DF, Sigurdsson A, Jonasdottir A, Jonasdottir A, Oddsson A, Helgason A, Magnusson OT, et al. 2013. Nonsense mutation in the LGR4 gene is associated with several human diseases and other traits. *Nature* **497**: 517–20. http://dx.doi.org/10.1038/nature12124 (Accessed March 24, 2014).

Threadgill DW, Hunter KW, Williams RW. 2002. Genetic dissection of complex and quantitative traits: from fantasy to reality via a community effort. *Mamm Genome* **13**: 175–8. http://www.ncbi.nlm.nih.gov/pubmed/11956758 (Accessed February 19, 2014).

Trapnell C, Pachter L, Salzberg SL. 2009. TopHat: discovering splice junctions with RNA-Seq. *Bioinformatics* **25**: 1105–11. http://www.ncbi.nlm.nih.gov/pubmed/19289445 (Accessed December 16, 2016).

Trikalinos TA, Salanti G, Zintzaras E, Ioannidis JPA. 2008. Meta-analysis methods. *Adv Genet* **60**: 311–34. http://www.ncbi.nlm.nih.gov/pubmed/18358326 (Accessed June 20, 2016).

Udagawa N, Takahashi N, Akatsu T, Tanaka H, Sasaki T, Nishihara T, Koga T, Martin TJ, Suda T. 1990. Origin of osteoclasts: mature monocytes and macrophages are capable of differentiating into osteoclasts under a suitable microenvironment prepared by bone marrow-derived stromal cells. *Proc Natl Acad Sci U S A* **87**: 7260–4. http://www.ncbi.nlm.nih.gov/pubmed/2169622 (Accessed December 10, 2016).

van der Kraan PM, Davidson ENB. 2015. Cross-talk between bone morphogenetic proteins and inflammatory pathways. *Arthritis Res Ther* **17**: 326. http://www.ncbi.nlm.nih.gov/pubmed/26592526 (Accessed June 26, 2016).

Verga Falzacappa MV, Casanovas G, Hentze MW, Muckenthaler MU. 2008. A bone morphogenetic protein (BMP)-responsive element in the hepcidin promoter controls HFE2-mediated hepatic hepcidin expression and its response to IL-6 in cultured cells. *J Mol Med (Berl)* **86**: 531–40. http://www.ncbi.nlm.nih.gov/pubmed/18421430 (Accessed November 18, 2015).

Wang Q, Xue M-L, Zhao G-Q, Liu M-G, Ma Y-N, Ma Y. 2015. Form-deprivation myopia induces decreased expression of bone morphogenetic protein-2, 5 in guinea pig sclera. *Int J Ophthalmol* **8**: 39–45. http://www.pubmedcentral.nih.gov/articlerender.fcgi?artid=4325239&tool=pmcentrez&rendertype=abstract (Accessed May 3, 2016).

Wu L, Wary KK, Revskoy S, Gao X, Tsang K, Komarova YA, Rehman J, Malik AB. 2015. Histone Demethylases KDM4A and KDM4C Regulate Differentiation of Embryonic Stem Cells to Endothelial Cells. *Stem cell reports* **5**: 10–21. http://www.sciencedirect.com/science/article/pii/S2213671115001599 (Accessed February 8, 2016).

Yalcin B, Flint J, Mott R. 2005. Using progenitor strain information to identify quantitative trait nucleotides in outbred mice. *Genetics* **171**: 673–81. http://www.genetics.org/content/171/2/673.short (Accessed April 24, 2014).

Yi T, Lee H-L, Cha J-H, Ko S-I, Kim H-J, Shin H-I, Woo K-M, Ryoo H-M, Kim G-S, Baek J-H. 2008. Epidermal growth factor receptor regulates osteoclast differentiation and survival through cross-talking with RANK signaling. *J Cell Physiol* **217**: 409–422. http://www.ncbi.nlm.nih.gov/pubmed/18543257 (Accessed December 10, 2016).

Zhang X, Zhang J, Bauer A, Zhang L, Selinger DW, Lu CX, Ten Dijke P. 2013. Fine-tuning BMP7 signalling in adipogenesis by UBE2O/E2-230K-mediated monoubiquitination of SMAD6. *EMBO J* **32**: 996–1007. http://www.pubmedcentral.nih.gov/articlerender.fcgi?artid=3616286&tool=pmcentrez&rendertype=abstract (Accessed February 15, 2016).